Chemistry & Biodiversity

WILEY-VCH

CHEMISTRY & BIODIVERSITY

RESEARCH ARTICLE

Synthesis, Antibacterial, and Antibiofilm Activities of Imidazo[2,1-b]Thiazole Chalcone Derivatives: In Vitro and In Silico Studies

Mohamed Azzouzi[1] | Mohamed El Boutaybi[1] | El Hassan El Majidi[1] | Mohammed Timinouni[2] | Lamiae El Khattabi[2] | Khadim Dioukhane[2] | Sofia Fait[2] | Adyl Oussaid[1]

[1]Laboratory of Molecular Chemistry, Materials and Environment (LCM2E), Department of Chemistry, Multidisciplinary Faculty of Nador, University Mohamed I, Nador, Morocco | [2]Laboratoire de Biotechnologie et Bioinformatique, Ecole des Hautes Etudes de Biotechnologie et de santé (EHEB), Casablanca, Morocco

Correspondence: Mohamed Azzouzi (azzouzi.mohamed@ump.ac.ma)

Received: 25 October 2024 | **Revised:** 3 January 2025 | **Accepted:** 13 January 2025

Funding: The authors received no specific funding for this work.

Keywords: antibacterial | antibiofilm | computational chemistry | green chemistry | imidazothiazole–chalcone

ABSTRACT

In recent years, imidazothiazole–chalcone conjugates have emerged as notable pharmacophores with potential applications in discovering biologically active compounds. This study focuses on synthesizing novel imidazo[2,1-b]thiazole chalcone derivatives through a facile and conventional process adhering to several principles of green chemistry, facilitating scalable production. The synthesized compounds underwent comprehensive spectroscopic analysis, including ^{1}H NMR, ^{13}C NMR, LC–MS, and FT-infrared (IR) techniques. Theoretical FT-IR and NMR analysis, frontier molecular orbitals (FMOs), and global reactivity descriptors were calculated and interpreted. Furthermore, molecular electrostatic potential (MEP) surface, Mulliken atomic charge, electron localization function (ELF), localized orbital locator (LOL), and quantum theory of atoms in molecules (QTAIM) were analyzed. The newly synthesized compounds were screened in vitro for their antibacterial and antibiofilm activities. In addition, computational docking studies were performed to gain further insights into molecular interactions and found to support the results.

1 | Introduction

Heterocyclic compounds, which contain at least one carbon atom and one heteroatom, such as nitrogen, oxygen, or sulfur, play a crucial role in various biological processes. Owing to their diverse pharmacological and therapeutic implications, fused heterocyclic compounds with five or six members have gained significant attention in medicinal chemistry [1]. Imidazothiazole is a biologically active fused heterocyclic scaffolding that constitutes a substantial class of nitrogen- and sulfur-bridged heterocyclic compounds that play a key role in medicinal chemistry [2]. Due to its vast array of applications, therapeutic properties, and ability to bind easily with receptors and enzymes [3], imidazothiazole scaffolds are one of the most significant derivatives in pharmaceuticals [4a, 4b, 4c, 4d]. The fused heterocycle imidazo[2,1-b] thiazole core exhibits well-known therapeutic properties, such as antitumor [5], anticancer [6a, 6b, 6c], antimicrobial [4c, 7], antiviral [8], antifungal [9a, 9b], anti-hypertensive [10], anti-inflammatory [11], and antipsychotic [12]. In addition, these therapeutic agents could effectively cure various diseases [13a, 13b]. This moiety has caught the interest of medicinal chemists due to its broad range of biological activities and occupies a prominent place in medicinal chemistry.

Recently, the medicinal properties of imidazothiazole and chalcone moieties have gained recognition as essential pharmacophores possessing multiple medicinal properties [14a, 14b]. Many studies have confirmed their excellent bioavailability and tolerance in the human body [15a, 15b]. Consequently, researchers worldwide are focused on synthesizing diverse derivatives to develop novel and more potent drugs for treating severe diseases such as cancer, diabetes, HIV, tuberculosis, and malaria [6a, 14a, 15a, 16a, 16b].

Nowadays, computational methodologies have become indispensable in drug discovery and development [17]. Density functional theory (DFT) and molecular docking studies are particularly noteworthy for their roles in elucidating the electronic structures of molecules and predicting their interactions with biological targets [18]. DFT provides detailed insights into the electronic properties of compounds [19], aiding in the understanding of their stability, reactivity, and potential biological activity [20]. Molecular docking simulations facilitate the prediction of how small molecules, such as drugs, interact with target proteins, thereby informing the design of compounds with enhanced efficacy and specificity [21]. The integration of these computational techniques with experimental approaches accelerates the identification and optimization of novel therapeutic agents, offering a more efficient pathway in the development of treatments for various diseases.

Due to the remarkable properties exhibited by both imidazo[2,1-b]thiazole and chalcone derivatives, we present the synthesis of novel imidazo[2,1-b]thiazole-based chalcone derivatives as a moiety that combines both active pharmacophores in a single scaffold. The synthesis approach employs several principles of green chemistry and allows for efficient and scalable production. The DFT method was used for a theoretical spectroscopic investigation, confirming and validating the structural assignment of the newly synthesized compounds. Additionally, reactivity descriptors, including highest occupied molecular orbital (HOMO) and lowest unoccupied molecular orbital (LUMO) molecular orbital energy values, ΔE_{gap}, chemical hardness (η), chemical softness (σ), electronegativity index (χ), molecular dipole moment (μ), and global electrophilicity index (ω), were computed to deepen our understanding of the compound's electronic structure. Molecular electrostatic potential (MEP), Mulliken atomic charge, electron localization function (ELF), localized orbital locator (LOL), and quantum theory of atoms in molecules (QTAIM) analyses were carried out and investigated to understand and predict the compound's chemical behavior. The newly synthesized derivatives were tested in vitro for their antibacterial and antibiofilm activities against *Escherichia coli*, *Klebsiella pneumoniae*, *Pseudomonas aeruginosa*, and *Staphylococcus aureus*. Furthermore, molecular docking studies targeting the DNA gyrase subunit B of *E. coli* were conducted to predict the potential binding interactions.

2 | Materials and Methods

2.1 | Chemicals and Instrumentation

All chemicals used were of reagent grade and utilized without further purification. Reaction progress was monitored by TLC. NMR spectra for both ^{1}H and ^{13}C were recorded using a JNM-ECZ500R/S1 FT NMR system (JEOL) operating at 500 MHz for ^{1}H and 126 MHz for ^{13}C. Chemical shifts are reported in parts per million (ppm) relative to the residual solvent peak used as an internal reference. Mass spectra were acquired with a Thermo Scientific TSQ 8000 Evo Triple Quadrupole GC-MS/MS system. The FT-infrared (IR) spectra were obtained using a JASCO FT/IR-4700 spectrometer over the range 4000–400 cm^{-1}. Purity was determined by Shimadzu LC-20 HPLC system. Melting points were determined using a Stuart SMP20 melting point apparatus.

2.2 | Synthesis

2.2.1 | General Synthesis Method for Precursors 2, 4, and 5

Initially, to a solution of 1 (4′-chloroacetophenone, 0.1 mol) and 0.2 mol of 30% H_2O_2 in H_2O (100 mL), 0.1 mol of 48% solution of HBr was added dropwise and kept overnight at ambient temperatures. The resulting product was filtered and washed with cold ether to obtain compound 2 (2-bromo-4′-chloroacetophenone). The preparation of 4 (6-(4-chlorophenyl)imidazo[2,1-b]thiazole) involved the condensation of 2 (0.1 mol) with 3 (2-aminothiazole, 0.1 mol) in 50 mL ethanol, which was stirred at 60°C for 8 h . After cooling, ethanol was removed in a vacuum, and the residue was poured into cold water (100 mL) and alkalinized to a basic pH. The mixture was extracted with DCM (3×30 mL^2), dried over anhydrous $MgSO_4$, and concentrated to yield compound 4, which was not further purified and directly subjected to Vilsmeier–Haack formylation by the reaction of $POCl_3$ (0.1 mol), which was added dropwise to a solution of DMF (0.1 mol) at 0°C stirred for a few minutes, resulting in the formation of an orange color solution. Next, 4 (0.1 mol) was added slowly while stirring, and 0°C temperature was maintained for 1 h and then refluxed for 6 h at 80°C. The reaction mixture was cooled, and the resulting product was filtered and washed with cold ethanol to give a sufficiently pure formylated product 5 (6-(4-chlorophenyl)imidazo[2,1-b]thiazole-5-carbaldehyde) that was utilized in the subsequent step without requiring additional purification.

2.2.2 | General Method of Synthesis of Chalcone of Imidazothiazole 7a–c

A mixture of intermediate product 5 (0.01 mol), and appropriate acetophenones 6 (0.01 mol) was mixed in ethanol with 1 mL of 10% aqueous KOH and stirred overnight at room temperature. The progress of the reaction was monitored by TLC. Upon its completion, the resulting compound was isolated by filtration and washed with hot ethanol, yielding the desired product in a good yield and high purity. Scheme 1 depicts a general strategy for synthesizing the target compounds.

2.3 | Computational Details

The software Gaussian 09W was employed to carry out the required DFT calculations. Gaussian calculations are carried out using the B3LYP/6-311++G (d, p) basis set. To identify the binding regions and reactive sites, a wave functional analysis was carried

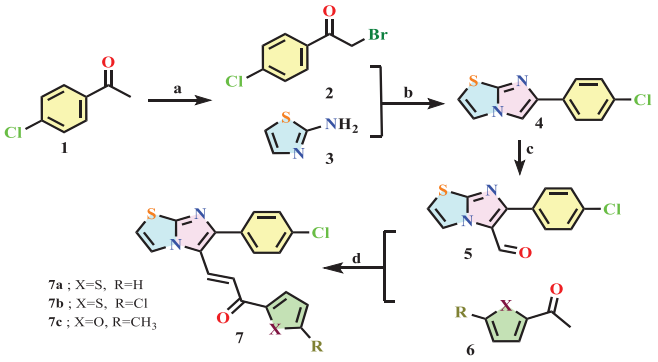

SCHEME 1 | Synthesis of compounds **7a–7c**. Reagents and conditions: (a) 48% HBr, 30% H_2O_2, H_2O, rt,24 h; (b) ethanol, reflux, 8 h; (c) $POCl_3$, DMF, reflux, 6 h; (d) 10% KOH, ethanol, RT, 24 h.

out using the Multiwfn program with the help of the wfn file of the optimized geometry [22].

2.4 | Antibacterial Activity

In this study, the antibacterial activity was tested against four reference bacterial strains (*E. coli* ATCC 25922*, K. pneumoniae* ATCC 13883, *S. aureus* ATCC 25923, and *P. aeruginosa* ATCC 27853). The inoculum suspension was obtained by taking colonies from 24-h cultures. The colonies were suspended in a sterile 0.9% aqueous solution of NaCl. The density was adjusted to the turbidity of a 0.5 McFarland Standard (10^8 colony-forming unit [CFU]/mL).

2.5 | Determination of Minimum Inhibitory Concentration (MIC) and Minimum Bactericidal Concentration (MBC)

The MIC is defined as the lowest concentration of an antimicrobial agent required to inhibit the visible growth of microorganisms after 24 h of incubation. MIC determination was performed using the broth micro-dilution method in 96-well microtiter plates, following the established protocol [23]. After separating the bacterial suspension, an overnight culture was adjusted to a final concentration of 10^8 CFU/mL in Mueller–Hinton broth (MHB). Serial dilutions of the tested compounds, ranging from 3.2 to 0.0125 mg/mL, were prepared in MHB with DMSO as the solvent. MHB with bacterial inoculum served as the positive control (T^+), whereas MHB with DMSO alone was used as the negative control (T^-). The microtiter plates were incubated at 37°C for 24 h.

As the compounds are colored, visually assessing turbidity, "the standard indicator of bacterial growth," can be challenging. To prevent misinterpretation and ensure accurate MIC determination, an additional step was incorporated. After incubation, 20 µL of the culture from each well was spread onto Luria Bertani (LB) agar plates, a nutrient-rich medium conducive to bacterial growth. The plates were subsequently incubated at 37°C for 24 h. The presence or absence of bacterial colonies on the LB agar provided a clear, unambiguous indication of bacterial growth or inhibition at each concentration tested. To enhance accuracy, all experiments were conducted in triplicate, and consistent results were observed across replicates, reinforcing the reliability of the findings. This approach minimized the risk of error introduced by the compound's color and ensured precise assessment of antibacterial activity.

The MBC is the lowest concentration of the antimicrobial agent capable of reducing 99.9% of the initial bacterial population after 24 h. It was determined as reported by Moreira et al. [24].

2.6 | Biofilm Formation Assay

Biofilm formation was assessed using the microtiter plate method with crystal violet staining, as described by Toole et al. [25]. Briefly, 200 µL of diluted bacterial culture was added to each well of a sterile 96-well flat-bottom polystyrene plate and incubated at 37°C for 24 h under static conditions. After incubation, non-adherent cells were removed by washing the wells three times with phosphate-buffered saline (PBS, pH 7.4). The biofilm biomass was then stained with 0.1% (w/v) crystal violet for 20 min at room temperature.

2.7 | Molecular Docking Analysis

2.7.1 | Compounds Preparation and Target Protein Selection

The 2D and 3D structures of the synthesized compounds were generated from the previously optimized structures using the Open Babel program. The molecular geometries were visualized and confirmed using PyMOL, ensuring accuracy and structural integrity. The finalized structures were saved in Protein Data Bank (PDB) format and subsequently converted to PDBQT file format using AutoDockTools 1.5.7. The DNA gyrase subunit B of *E. coli* (strain K12) was chosen as the target enzyme for this study due to its essential role in bacterial DNA replication and its significance as an antibacterial target. The protein structure was obtained from the PDB (ID: 4PRX), with a resolution of 1.800 Å [26]. Protein preparation involved removing heteroatoms, water molecules, and cofactors, followed by assigning Gasteiger charges and polar hydrogens. The processed protein structure was saved in PDBQT file format using AutoDockTools 1.5.7, ensuring compatibility with docking simulations [26].

2.7.2 | Molecular Docking

Molecular docking studies were performed using AutoDock Vina to predict the binding affinities of the synthesized compounds to the active site of DNA gyrase subunit B. The active site was defined by centering the grid box at coordinates $x = -13.85$, $y = -48.58$, and $z = -9.11$, based on prior studies [26]. The docking scores, expressed in kcal/mol, were used to quantify the binding affinities of the compounds [26, 27].

2.7.3 | Visualization and Data Analysis

The docking scores obtained from AutoDock Vina were tabulated and analyzed to determine the relative binding affinities of

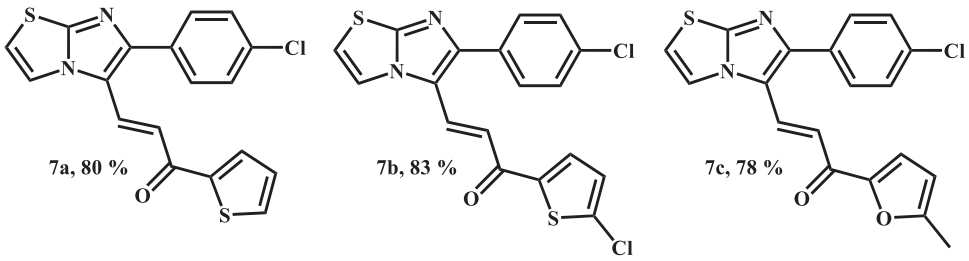

FIGURE 1 | Chemical structures of compounds **7a–c**.

7a–c. The results were visualized using BIOVIA Discovery Studio to depict the interaction of each molecule within the active site of the enzyme. Figures were generated to illustrate the 2D and 3D structures of the molecules, the target protein, and the docking poses of the compounds in the active site [28].

3 | Results and Discussion

3.1 | Chemistry

In this study, imidazo[2,1-b]thiazole-based chalcones were synthesized using a simple and efficient synthetic approach. Initially, the intermediate 4 (6-(4-chlorophenyl)imidazo[2,1-b]thiazole) was obtained by the condensation of 2 (2-bromo-4′-chloroacetophenone) with 3 (2-aminothiazole) [6b]. A Vilsmeier–Haack treatment on the fused heterocycles 4 yielded the formylated product 5 (6-(4-chlorophenyl)imidazo[2,1-b]thiazole-5-carbaldehyde) [29]. Novel chalcone derivatives were prepared by Claisen–Schmidt condensation by reacting formylated product 5 with different methyl ketones to give the corresponding α,β-unsaturated ketones **7a–c** as pure products in good yields [6a]. All novel synthesized chalcones were fully characterized. ^{1}H, ^{13}C NMR, LC-MS (ESI), HPLC chromatograms, and FT-IR spectra can be found in the Supporting Information Section.

3.1.1 | (E)-3-(6-(4-Chlorophenyl)imidazo[2,1-b]thiazol-5-yl)-1-(thiophen-2-yl)prop-2-en-1-one 7a

Obtained from 2-acetyl thiophene as a yellow powder; yield 80%, mp; 218°C–220°C, RMN ^{1}H (500 MHz, $CDCl_3$) δ 8.02 (d, J = 15.4 Hz, 1H), 7.84 (d, J = 4.5 Hz, 1H), 7.77 (d, J = 3.8 Hz, 1H), 7.66 (d, J = 4.9 Hz, 1H), 7.65 (d, J = 8.5 Hz, 2H), 7.44 (d, J = 8.5 Hz, 2H), 7.17 (dd, J = 4.9, 3.8 Hz, 1H), 7.14 (d, J = 15.4 Hz, 1H), 7.08 (d, J = 4.5 Hz, 1H). RMN ^{13}C (126 MHz, $CDCl_3$) δ 181.32, 153.87, 152.33, 145.48, 135.04, 133.78, 132.07, 131.39, 130.29, 129.76, 129.16, 128.42, 120.53, 119.42, 116.68, 114.54. FT-IR: υ(C–H) = 3126, 3095 cm^{-1}; υ(C = O) = 1644 cm^{-1}; υ(C = C) = 1566 cm^{-1}; υ(C = N) = 1413 cm^{-1}; υ(C–N) = 1244 cm^{-1}; υ(C–C) = 1060 cm^{-1}; υ(C–Cl) = 812 cm^{-1}. LC–MS: m/z = 371.006 (M + 1).

3.1.2 | (E)-3-(6-(4-Chlorophenyl)imidazo[2,1-b]thiazol-5-yl)-1-(5-chlorothiophen-2-yl)prop-2-en-1-one 7b

Obtained from 2-acetyl-5-chlorothiophene as a golden powder; yield 83%, mp; 209°C–211°C, RMN ^{1}H (500 MHz, DMSO-D_6) δ 8.67 (d, J = 4.5 Hz, 1H), 8.30 (d, J = 4.1 Hz, 1H), 7.75 (d, J = 15.5 Hz, 1H), 7.63 (d, J = 8.5 Hz, 2H), 7.59 (d, J = 4.5 Hz, 1H), 7.56 (d, J = 8.5 Hz, 2H), 7.38 (d, J = 15.5 Hz, 1H), 7.33 (d, J = 4.1 Hz, 1H). RMN ^{13}C (126 MHz, DMSO-D_6) δ 180.84, 154.67, 152.51, 145.17, 138.30, 134.14, 134.11, 132.67, 130.99, 129.56, 129.42, 129.12, 122.38, 120.61, 116.16, 115.06. FT-IR: υ(C–H) = 3141, 3100 cm^{-1}; υ (C = O) = 1639 cm^{-1}; υ(C = C) = 1579 cm^{-1}; υ(C = N) = 1417 cm^{-1}; υ(C –N) = 1248 cm^{-1}; υ (C–C) = 1018 cm^{-1}; υ(C–Cl) = 790 cm^{-1}. LC–MS: m/z = 405.971 (M + 1).

3.1.3 | (E)-3-(6-(4-Chlorophenyl)imidazo[2,1-b]thiazol-5-yl)-1-(5-methylfuran-2-yl)prop-2-en-1-one 7c

Obtained from 2-acetyl-5-methyl furan as an orange powder; yield 78%, mp; 150°C–152°C, RMN ^{1}H (500 MHz, $CDCl_3$) δ 8.01 (d, J = 15.8 Hz, 1H), 7.86 (d, J = 4.4 Hz, 1H), 7.65 (d, J = 8.6 Hz, 2H), 7.44 (d, J = 8.6 Hz, 2H), 7.18 (d, J = 3.5 Hz, 1H), 7.13 (d, J = 15.8 Hz, 1H), 7.07 (d, J = 4.5 Hz, 1H), 6.20 (d, J = 3.5 Hz, 1H), 2.43 (s, 3H). RMN ^{13}C (126 MHz, $CDCl_3$) δ 176.92, 157.88, 153.67, 152.69, 151.94, 134.92, 132.12, 130.29, 129.13, 128.99, 120.72, 119.57, 119.16, 116.70, 114.35, 109.63, 14.34. FT-IR: υ(C–H) = 3148, 3094, 2840 cm^{-1}; υ(C = O) = 1642 cm^{-1}; υ(C = C) = 1553 cm^{-1}; υ(C = N) = 1451 cm^{-1}; υ(C–N) = 1245 cm^{-1}; υ(C–C) = 1012 cm^{-1}; υ(C–Cl) = 811 cm^{-1}. LC–MS: m/z = 369.045 (M + 1) (Figure 1).

3.2 | Green Chemistry Metrics Calculations

To assess the environmental sustainability of the synthesized compounds, we conducted green metrics calculations using widely recognized metrics such as carbon efficiency (CE), atom economy (AE), reaction mass efficiency (RME), mass intensity (MI), and environmental impact factor (E-Factor). These criteria have been delivered over the last decade to evaluate the environmental impact of chemical processes and products to reduce theoretical waste and create more environmentally friendly processes and products. Among these metrics, the E-Factor has emerged as a critical measure for quantifying the environmental impact of chemical reactions. It is defined as the mass ratio of waste to the desired product, including byproducts, leftover reactants, solvent losses, and anything else that can be regarded as waste. Given the volatile nature of the used solvents and their recovery through a simple recycling step using a standard rotary evaporator, we ensured that the calculations did not include any amount of solvents that could be recycled or reused to avoid overestimating the waste generated during the reactions [30a, 30b]. In the following assessments, the green metrics were estimated following reported procedures (Table 1) [31a, 31b, 31c].

TABLE 1 | Green metrics calculations (including the stoichiometric coefficient).

Reactions	Compound	Yield (%)	CE (%)	AE (%)	RME (%)	MI	E-Factor
a.	2	98	98	76.93	75.48	1.32	0.32
b.	4	94	94	70.34	66.12	1.51	0.51
c.	5	91	78	56.98	51.84	1.92	0.92
d.	7a	86	86	95.41	81.81	1.22	0.22
	7b	92	92	95.74	88.24	1.13	0.13
	7c	81	81	95.34	77.32	1.29	0.29
Optimum value	—	100	100	100	100	1	0

Abbreviations: AE, atom economy; CE, carbon efficiency; E-Factor, environmental impact factor; RME, reaction mass efficiency.

The results presented in Table 1 indicate that the chemical reactions were conducted with a high degree of efficiency in terms of conversion of starting materials into the desired product with minimum waste exclusion. This is evidenced by the high CE, AE, and RME values, which indicate a high degree of selectivity in producing a large proportion of the desired product with minimal waste.

The MI and E-factor values also suggest that the reactions had a relatively low environmental impact, as the amount of waste generated per product unit was relatively low. This is an essential consideration for the ecological sustainability of the synthesized compounds, as the generation of waste can contribute to environmental pollution and resource depletion.

Overall, the results suggest that the synthesized compounds have high environmental sustainability, as the reactions were carried out with a high degree of efficiency and minimized waste generation. This is an important consideration for developing sustainable chemical processes and producing environmentally friendly products.

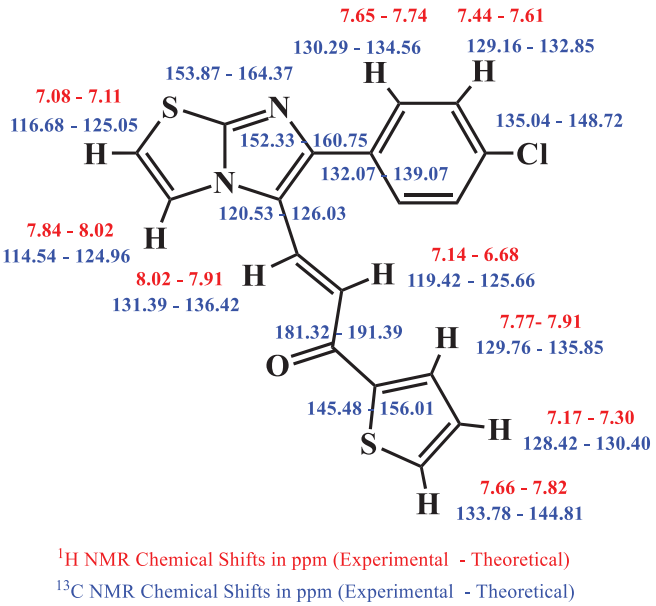

FIGURE 2 | Experimental and theoretical NMR chemical shifts of **7a**.

3.3 | ^{1}H and ^{13}C NMR Spectral Studies

NMR spectroscopy is one of the most important techniques for the structural analysis of organic compounds. The ^{1}H and ^{13}C chemical shifts, calculated through gauge-invariant atomic orbital (GIAO) method using the B3LYP function with the 6-311++ G(2d,p) basis set, were compared with experimentally observed NMR spectral values [32]. The experimental and theoretical NMR chemical shifts of the investigated compounds are given in Figures 2–4 for **7a**–**c**, respectively.

^{1}H NMR spectra of compound **7a** revealed the expected characteristic protons, displaying the presence of two doublets with a high coupling constant corresponding to protons of the functional group HC = CH of the formed α,ß-unsaturated ketone; the first appeared at δ 7.14 ppm, whereas the second appeared at δ 8.02 ppm, and theoretically calculated at 6.68 and 7.91 ppm, respectively. Moreover, the appearance of two doublets, the first at δ = 7.44 ppm and the other at δ = 7.65 ppm, is due to the aromatic protons of the benzyl group, which were theoretically observed at 7.61 and 7.65 ppm, respectively. Two doublets, one at δ = 7.08 ppm and the other at δ = 7.84 ppm, are attributable to the two protons of the thiophene ring and computed at 7.11 and 8.21 ppm, respectively. However, ^{13}C NMR spectra displayed a characteristic peak at δ 181.32 ppm corresponding to the C = O group, which was theoretically observed at 191.39. The benzyl carbons are experimentally observed at 129.16, 130.29, 132.07, and 135.04 ppm and calculated at 132.85, 134.56, 139.07, and 148.72 ppm. The imidazothiazole ring carbons were observed at 114.54, 116.68, 120.53, 152.33, and 153.87 ppm experimentally and at 124.96, 125.05, 126.03, 160.75, and 164.37 ppm theoretically. The experimental and calculated shifts of the thiophene ring were observed experimentally at 128.42, 129.76, 133.78, and 145.48 ppm and theoretically at 130.40, 135.85, 144.81, and 156.01 ppm. The chemical shifts of the HC = CH of the α,ß-unsaturated ketone are established at 119.42 and 131.93 ppm, and the theoretical δ values are 125.66 and 136.42 ppm.

Similarly, the ^{1}H NMR experimental spectrum of **7b** displayed two doublets corresponding to olefinic protons at 7.38 and 7.75 ppm and theoretically observed at 6.59 and 7.87 ppm, also the presence

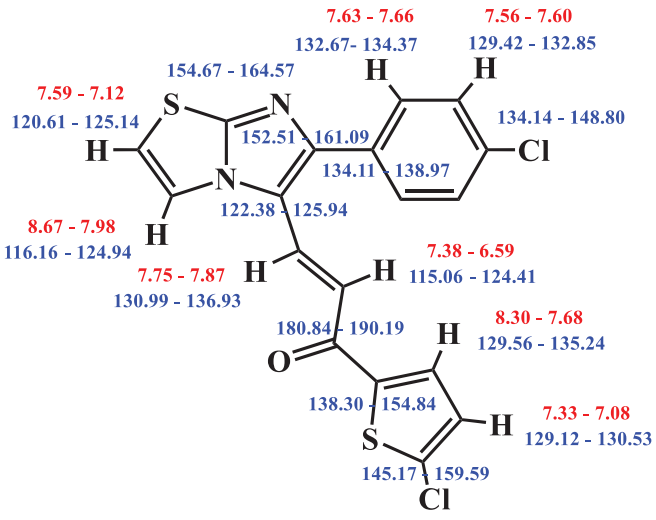

FIGURE 3 | Experimental and theoretical NMR chemical shifts of **7b**.

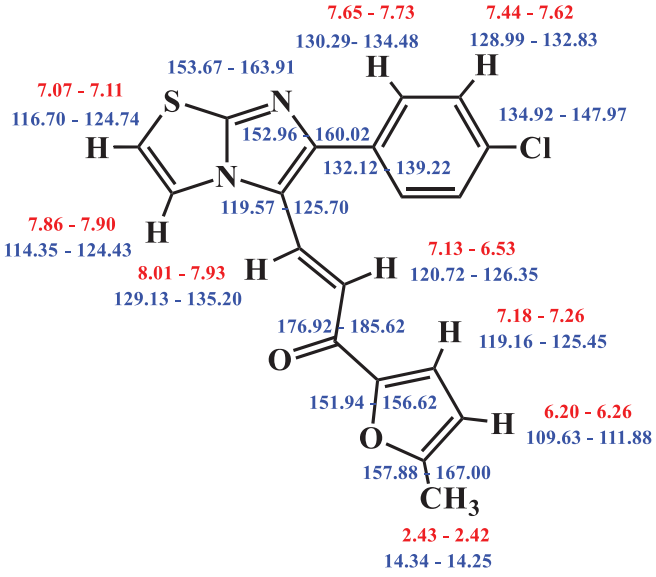

FIGURE 4 | Experimental and theoretical NMR chemical shifts of **7c**.

of two doublets at δ = 7.56 ppm and δ = 7.63 ppm due to the aromatic protons of the benzyl group, which were theoretically computed at 7.60 and 7.66 ppm. Moreover, two doublets at δ = 7.59 ppm and 8.67 ppm were observed experimentally for the thiazole ring protons and theoretically at 7.12 and 7.59 ppm. Finally, two doublets at δ = 7.33 ppm and δ = 8.30 ppm correspond to the two thiophene protons, whereas theoretical values were 7.08 and 7.68 ppm. Moreover, additional confirmation was obtained by the ^{13}C NMR spectrum with a characteristic peak at δ = 180.84 ppm due to C = O, which confirmed the formation of the predicted prop-2-en-1-one derivatives, whereas it was 190.19 ppm for theoretical ^{13}C NMR. The peaks appeared experimentally at 129.42, 132.67, 134.11, and 148.80 ppm and are assigned to the benzyl carbons, which were theoretically observed at 132.85, 134.73, 138.97, and 148.80 ppm. The peaks of the imidazothiazole ring carbons were observed at 116.16, 120.61, 122.38, 152.51, and 154.67 ppm and predicted at 124.94, 120.61, 122.38, 152.51, and 154.67 ppm. In thiophene ring, the experimental chemical shifts of carbon atoms were observed at 129.12, 129.56, 138.30, and 145.17 ppm and calculated at 130.53, 135.24, 154.84, and 159.59 ppm. The signals at 115.06 and 130.99 ppm were assigned experimentally to carbon atoms of the functional group HC = CH, and calculated values were obtained at 124.41 and 136.96 ppm.

Furthermore, ^{1}H NMR analysis of compound 7c demonstrated the appearance of coupling between the two olefinic protons, where two doublet signals appeared at δ = 7.13 and 8.01 ppm and calculated at 6.53 and 8.01 ppm. The experimental chemical shifts ascribed to aromatic protons of the benzyl group occurred at 7.44 and 7.65 ppm and in simulated spectra, they were observed at 7.62 and 7.65 ppm. The appearance of two doublets at δ = 7.07 and 7.86 ppm is attributable to the two protons of the furan ring, which were theoretically observed at 7.11 and 7.90 ppm. Moreover, ^{1}H NMR spectra displayed a singlet at δ = 2.43 ppm clearly corresponding to the CH_3 group attached to the furan ring, which shows excellent agreement with the calculated value at 2.42 ppm, in addition to two doublets at δ = 6.20 ppm and δ = 7.18 ppm attributable to the two protons of the same ring, which agrees with calculated values identified at 6.26 and 7.26 ppm.

Moreover, ^{13}C NMR spectra of **7c** showed a peak δ = 176.92 ppm experimentally and 185.62 ppm theoretically corresponding to C = O group. Moreover, the benzyl carbons chemical shifts are identified at 128.99, 130.29, 132.12, and 134.48 ppm, which were theoretically observed at 132.83, 134.48, 132.12, and 147.97 ppm. The peaks of the imidazothiazole ring carbons were measured at 119.57, 124.43, 124.74, 152.96, and 153.67 ppm and predicted at 125.70, 124.43, 124.74, 160.02, and 163.91 ppm. The experimental and calculated shifts of furan ring were observed experimentally at 109.63, 119.16, 151.91, and 157.88 ppm and theoretically at 111.88, 125.45, 156.62, and 167.00 ppm. The signal at 120.72 and 129.13 ppm were assigned experimentally to carbon atoms of the functional group HC = CH, and calculated values were obtained at 126.35 and 135.20 ppm. The chemical shifts of the HC = CH of the α,ß-unsaturated ketone are established at 119.42 and 131.93 ppm and the theoretical δ values are 125.66 and 136.42 ppm. The signal at 14.34 ppm assigned to the carbon of the methyl group attached to the furan ring, which correlated well with the theoretical shift obtained at 14.25 ppm.

Although the calculated NMR chemical shifts closely align with experimental values, minor deviations are observed. These deviations can be attributed to intra-molecular hydrogen bonding and specific interactions with solvent molecules or neighboring molecules, which are not included in the computational model. It should be noted that the theoretical chemical shifts were obtained for structures frozen in the gas phase, where molecular rotations are restricted, unlike in solution-phase environments. This restriction leads to the averaging of chemical shifts in experimental data, accounting for observed differences.

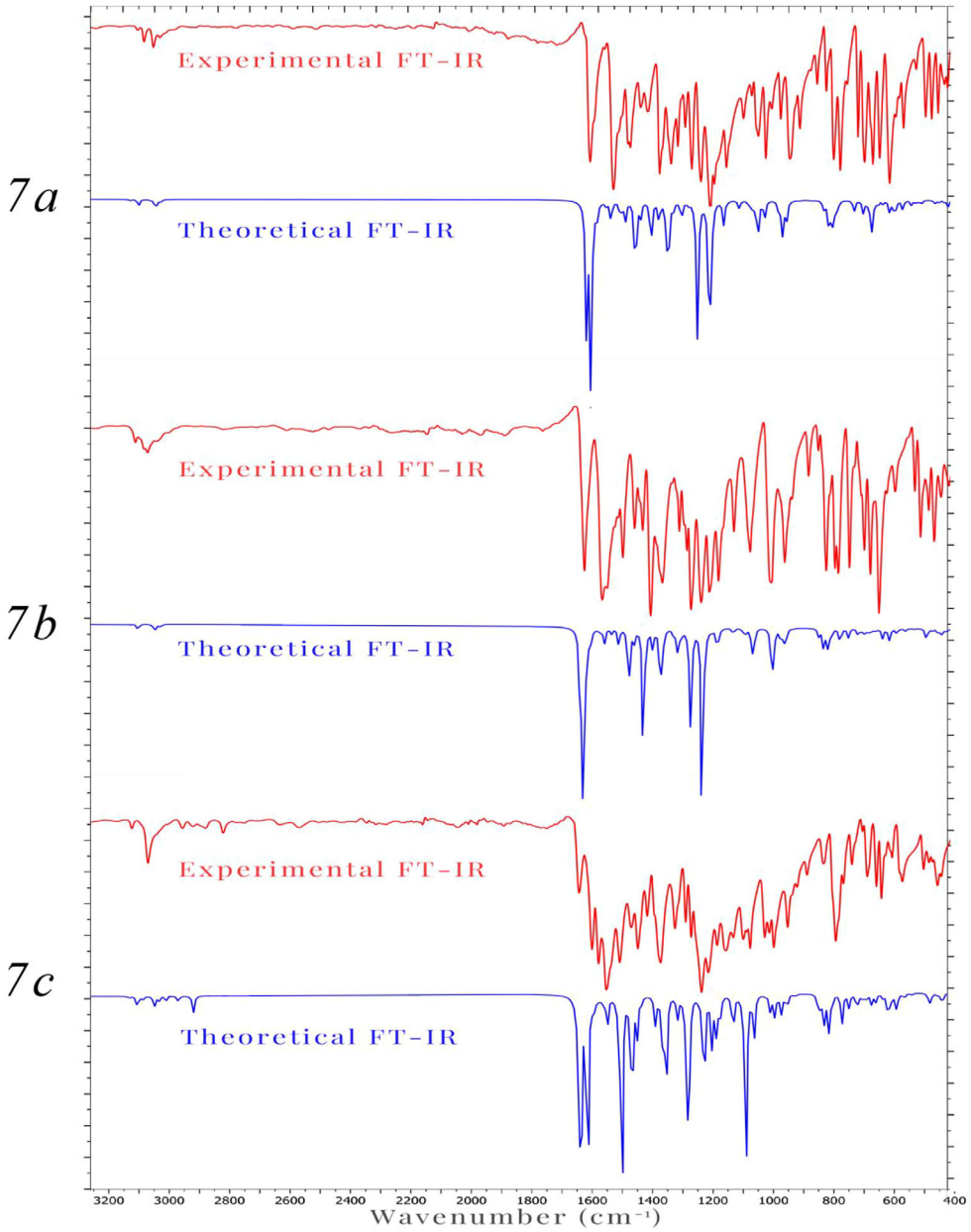

FIGURE 5 | Experimental FT-IR and theoretical FT-IR spectra of **7a–c**.

3.4 | Vibrational Analysis

The synthesized compounds were subjected to IR spectral analysis, and both the experimental and theoretical FT-IR spectra are presented in Figure 5. Vibrational frequencies were determined on the basis of the optimized structural parameters, with theoretical IR frequencies visualized using the GaussView 6.0 software. After applying a scaling factor of 0.961 to the calculated wavenumbers, good correlation was obtained between the experimental and theoretical IR spectra.

3.4.1 | C–H Vibrations

Literature reports indicate that C–H stretching vibrations generally fall within the range of 3100–3000 cm^{-1} [28]. In this investigation, the experimental spectrum displayed C–H stretching frequencies between 3126 and 3095 cm^{-1} for **7a**, between 3141 and 3100 cm^{-1} for **7b**, and between 3148 and 2839 cm^{-1} for **7c**, respectively. However, the calculated (C–H) stretching vibrations were determined at 3133 and 3064 cm^{-1} for **7a**, between 3133 and 3079 cm^{-1} for **7b**, and between 3159 and 2912 cm^{-1} for **7c**, respectively.

3.4.2 | C = O Vibrations

Literature data suggest that C = O stretching vibrations typically occur within the 1800–1600 cm^{-1} range [33]. In this study, the C = O stretching frequencies were observed at 1644, 1639, and 1642 cm^{-1} for **7a–c**, respectively. However, in the computed spectrum, the (C = O) stretching bands were recognized at 1601, 1598, and 1613 cm^{-1} for **7a–c**, respectively.

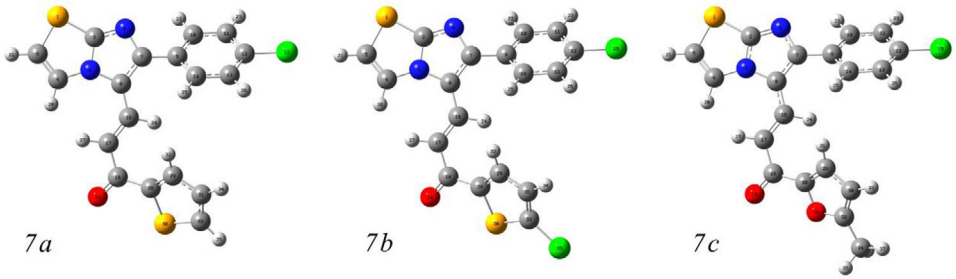

FIGURE 6 | The optimized molecular structures of **7a–c**.

3.4.3 | C = C Vibrations

According to the literature, C = C stretching vibrations typically fall within the 1650–1200 cm^{-1} range [34]. For the studied compounds, the theoretical stretching vibration bands were calculated to lie between 1587 and 1479 cm^{-1} for **7a**, 1587 and 1502 cm^{-1} for **7b**, and 1590 and 1482 cm^{-1} for **7c**. In the experimental spectra, the C = C stretching vibrations were observed between 1566 and 1509 cm^{-1} for **7a**, between 1579 and 1509 cm^{-1} for **7b**, and between 1599 and 1509 cm^{-1} for **7c**.

3.4.4 | C = N Vibrations

The literature reports a range of 1689–1471 cm^{-1} for the C = N stretching vibrations [35]. In the present molecules, the stretching vibration bands were recorded at 1413, 1417, and 1451 cm^{-1} for **7a–c**, respectively. In the calculated spectrum, 1446, 1446, and 1447 cm^{-1} vibrations were assigned to the (C = N) stretching bands in **7a–c**, respectively.

3.4.5 | C–N and C–C Vibrations

Assigning the (C–N) and (C–C) vibrations can be complex due to their overlap within a crowded spectral region featuring multiple bands. According to the literature, (C–N) stretching vibrations are generally observed between 1360 and 1000 cm^{-1} [36], whereas (C–C) vibrations typically appear in the range of 1590–1000 cm^{-1} [37]. In the compounds under investigation, the calculated (C–N) modes were identified at 1340, 1229, and 1211 cm^{-1} for **7a**, whereas the (C–C) mode was noted at 1249 cm^{-1}. For **7b**, the (C–N) modes were found at 1347, 1341, and 1230 cm^{-1}, with (C–C) modes at 1478 and 1250 cm^{-1}. In **7c**, the (C–N) modes appeared at 1348 and 1216 cm^{-1}, and the (C–C) mode was identified at 1268 cm^{-1}.The experimental spectra revealed vibrations assigned to (C–N) and (C–C) stretching bands, observed between 1244 and 1060 cm^{-1} for **7a**, 1248 and 1018 cm^{-1} for **7b**, and 1245 and 1012 cm^{-1} for **7c**.

3.5 | DFT Calculation Studies

3.5.1 | Geometry and Frontier Molecular Orbitals (FMOs) Investigations

DFT calculations were performed to gain deeper insight into the electronic structure, chemical reactivity, and molecular properties of the synthesized imidazo[2,1-b]thiazole-based chalcones. All calculations were carried out using the Gaussian 09W software package, employing the B3LYP functional and the 6-311++G(d,p) basis set. The optimized molecular geometries, electronic properties, and FMOs were examined to assess the reactivity of the synthesized compounds [38].

TABLE 2 | Global reactivity descriptors of **7a–c**.

Quantum parameters	7a	7b	7c
E_{HOMO} (eV)	−6.21263	−6.28311	−6.14351
E_{LUMO} (eV)	−2.54290	−2.66372	−2.41773
ΔE_{gap} (eV)	3.66973	3.61938	3.72578
η (eV)	1.83486	1.80969	1.86289
σ (eV^{-1})	0.54499	0.55257	0.53679
χ (eV)	4.37777	4.47341	4.28062
ω (eV)	5.22242	5.52896	4.91809
μ (Debye)	2.41298	3.88955	1.67880

The optimized structures of chalcones **7a–c** were obtained by DFT calculations, as shown in Figure 6. These calculations were conducted in the gas phase, meaning that the molecules were assumed to be in a vacuum, excluding solvent interactions and environmental effects. The optimized geometries reveal that the imidazo[2,1-b]thiazole ring and the chalcone moiety adopt a nearly coplanar conformation, with slight deviations in planarity depending on the substituents attached to the chalcone unit. The planarity of these conjugated systems is expected to enhance electronic delocalization across the molecule, contributing to the electronic properties and reactivity, as well as facilitating π–π stacking interactions, which play a significant role in the binding interactions with biological targets such as bacterial enzymes and DNA [39].

The HOMO and LUMO are key indicators of a molecule's chemical reactivity, with the energy gap (ΔE_{gap}) between these orbitals providing insight into the stability and potential for electron transfer [33]. For compounds **7a–c**, the HOMO and LUMO energy levels were computed and are presented in Table 2. These values were calculated relative to the vacuum level, which is commonly used as the reference point in computational chemistry. In this context, negative HOMO and LUMO energy levels indicate that the molecules are in a stable bound state compared to free electrons in a vacuum.

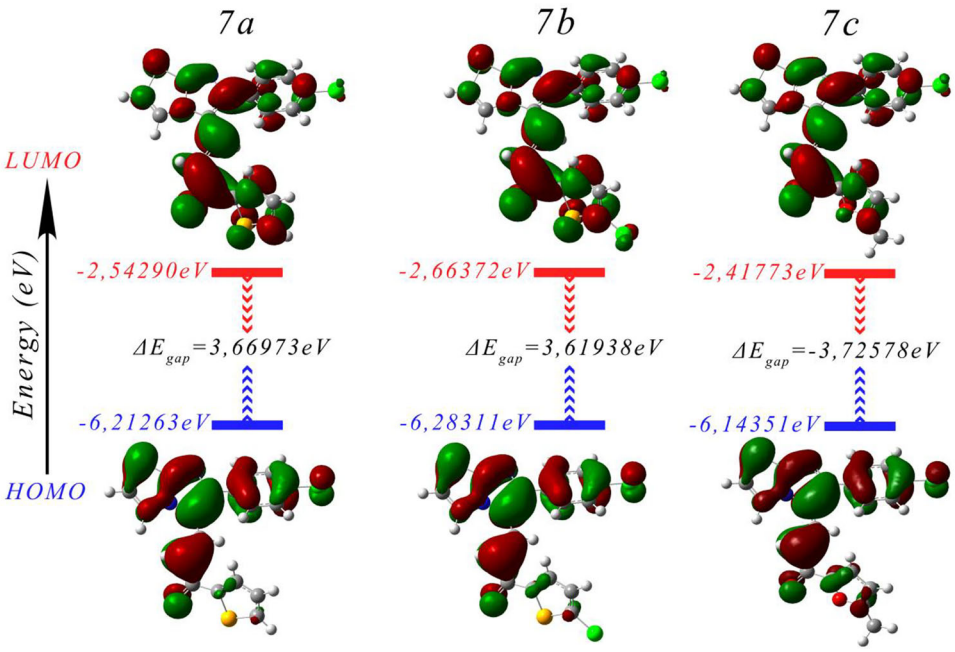

FIGURE 7 | Correlation diagram between HOMO and LUMO of **7a–c**. HOMO, highest occupied molecular orbital; LUMO, lowest unoccupied molecular orbital.

The HOMO–LUMO energy gaps for compounds **7a–c** were calculated as 3.67, 3.62, and 3.73 eV, respectively. These relatively small ΔE_{gap} values suggest that these compounds are chemically reactive and capable of undergoing charge transfer interactions, which are critical in many biological processes, including enzyme inhibition and bacterial cell membrane disruption. Among the three, compound **7b** exhibited the smallest energy gap (3.62 eV), indicating that it may be the most reactive and likely to interact strongly with biological targets [40].

Figure 7 illustrates the spatial distribution of the HOMO and LUMO orbitals for the synthesized chalcones. The HOMO orbitals are largely localized on the imidazo[2,1-b]thiazole core, suggesting that this region is electron-rich and likely to participate in electron donation during chemical reactions. In contrast, the LUMO orbitals are predominantly localized on the chalcone moiety, particularly around the carbonyl group and the phenyl ring, indicating that these regions are likely to accept electrons during interactions with biological molecules. This distribution of FMOs suggests that electron donation occurs from the imidazo[2,1-b]thiazole scaffold, whereas the chalcone unit serves as the primary site for electrophilic attack, which is important for understanding the mechanism of action of these compounds in biological systems.

Global reactivity descriptors, such as chemical hardness (η), chemical softness (σ), electronegativity (χ), and the electrophilicity index (ω), were calculated using the HOMO and LUMO energies. These descriptors provide valuable insights into the compounds' stability, reactivity, and ability to interact with biological systems [41].

The chemical hardness indicates a molecule's resistance to deformation of the electron cloud or, in other words, the resistance to charge transfer. The hardness values for compounds **7a–c** were calculated to be 1.83, 1.81, and 1.86 eV, respectively. A harder molecule is less reactive, whereas a softer molecule is more reactive. Compound **7b**, with the lowest hardness value (1.81 eV), is predicted to be the most reactive, which aligns with its observed antibacterial efficacy. Conversely, compound **7c**, with the highest hardness value (1.86 eV), is expected to be more stable but less reactive, which might explain its relatively lower biological activity [42].

Chemical softness is the inverse of hardness and is a measure of a molecule's ability to undergo chemical reactions by accepting or donating electrons. It is directly related to the molecule's reactivity. The softness values for compounds **7a–c** were 0.54, 0.55, and 0.53 eV^{-1}, respectively. Compound **7b** exhibited the highest softness value (0.55 eV^{-1}), suggesting it is the most reactive among the three compounds, making it a stronger candidate for interacting with biological targets, such as bacterial enzymes. In contrast, compound **7c** had the lowest softness (0.53 eV^{-1}), indicating relatively lower reactivity and interaction potential [43].

Electronegativity, another important descriptor, is a measure of the tendency of an atom or molecule to attract electrons toward itself. Higher electronegativity values suggest a molecule is more likely to accept electrons, making it a better electrophile. The electronegativity values for compounds **7a–c** were calculated as 4.38, 4.47, and 4.28 eV, respectively. Among these, compound **7b** exhibited the highest electronegativity (4.47 eV), indicating that it has a greater tendency to attract electrons and participate in electrophilic reactions [44]. This could explain its enhanced biological activity, as its higher electronegativity enables stronger interactions with nucleophilic sites in biological molecules, such as enzymes and proteins [45].

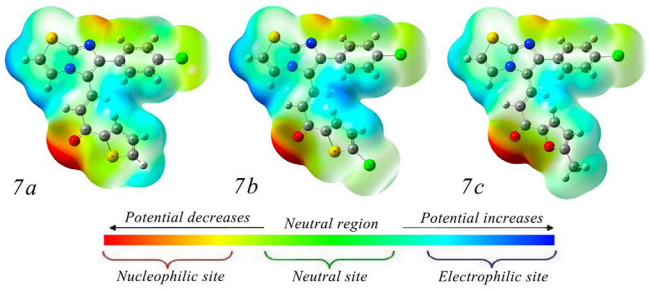

FIGURE 8 | MEP surface of **7a–c**.

The electrophilicity index quantifies the ability of a molecule to accept electrons. The electrophilicity values for compounds **7a–c** were 5.22, 5.53, and 4.92 eV, respectively. Compound **7b** had the highest electrophilicity (5.53 eV), suggesting it is the strongest electrophile among the three, making it more likely to engage in interactions with electron-rich sites in bacterial cells. This high electrophilicity index correlates well with the enhanced antibacterial and antibiofilm activities observed experimentally [46].

The computed values of global reactivity descriptors are consistent with the experimental observations, where compounds with lower ΔE_{gap} and higher electrophilicity showed better antibacterial and antibiofilm activities. This suggests that DFT calculations can serve as a reliable predictor of the biological potential of these chalcones.

3.5.2 | MEP Analysis

The MEP surfaces provide valuable information regarding the electron density distribution in a molecule, allowing the identification of potential reactive sites for electrophilic and nucleophilic attacks [47]. The MEP surfaces of **7a–c**, shown in Figure 8, illustrate areas of varying electrostatic potential, which are critical for understanding molecular interactions with biological targets.

For all compounds, the MEP analysis reveals that the regions of the most negative electrostatic potential (represented in red) are primarily localized around the oxygen atom of the carbonyl group in the chalcone moiety. This suggests that the carbonyl oxygen is a key site for nucleophilic interactions, such as hydrogen bonding or coordination with positively charged biological molecules. Additionally, there is a negative electrostatic potential around the nitrogen atom of the imidazole ring, further indicating its role as a nucleophilic site. In contrast, the most positive electrostatic potential (represented in blue) is centered around the hydrogen atoms attached to the carbon atoms between the imidazo[2,1-b]thiazole ring and the chalcone moiety, as well as in the vicinity of the thiazole sulfur atom. This positive potential highlights regions where electrophilic attack is likely to occur, particularly through interactions with electron-rich biological targets such as bacterial enzymes or DNA [48].

The electron density distribution observed in the MEP surfaces of these chalcone derivatives suggests that the molecules are well suited for interaction with both nucleophilic and electrophilic sites in biological systems. The localization of negative potential on the oxygen and nitrogen atoms facilitates strong hydrogen bonding interactions, whereas the positive potential regions make the compounds capable of engaging in π–π stacking interactions or other electrophilic reactions [49].

3.5.3 | Mulliken Charge Analysis

To further investigate the charge distribution within the molecules, Mulliken atomic charge analysis was conducted; this analysis aids in understanding the electronic environment around individual atoms [50]. The Mulliken charges of compounds **7a–c** depicted in Figure 9 reveal distinct patterns in the distribution of electron density. For all compounds, certain atoms display positive and negative charges, indicating electron-deficient and electron-rich regions, respectively. These regions can serve as potential sites for electrophilic and nucleophilic attacks [46].

In the imidazo[2,1-b]thiazole-based chalcone derivatives, carbon atoms exhibit varying degrees of charge, ranging from positive to negative values. For instance, carbon atoms C-2, C-7, C-9, C-12, and C-18 show positive charges, suggesting they are electron-deficient. This electron deficiency is likely due to electron withdrawal by more electronegative atoms or functional groups within the molecule. In contrast, carbon atoms C-4, C-11, C-16, and C-18 display relatively high negative charges, due to possible resonance effects or interaction with neighboring atoms [51].

Nitrogen atoms N-3 and N-6 in **7a** and **7b** show a positive charge, indicating electron deficiency, which could be attributed to their role in the conjugated ring system. On the other hand, nitrogen atom N-6 in **7c** carries a negative charge, indicating a higher electron density localized at this position [44]. The oxygen atom (O-19) and sulfur atom (S-1) exhibit negative charges, which is expected due to their electron-withdrawing nature [52]. This makes the oxygen and sulfur atom a key site for hydrogen bonding and nucleophilic interactions, particularly with biological receptors or enzymes [53]. Conversely, hydrogen atoms in the synthesized chalcones generally carry positive charges, indicating electron deficiency, which is a typical characteristic of hydrogen atoms in organic molecules [54].

3.5.4 | ELF and LOL Analyses

The ELF and LOL analyses were utilized to assess the electron pairing and distribution within the molecules [55]. As illustrated in Figure 10, areas of intense electron localization, highlighted in red, are primarily located around the hydrogen atoms of the imidazothiazole core and the hydrogen atoms in the functional group HC = CH of the α,β-unsaturated ketone. This indicates significant electron localization, which is typically associated with covalent bonding or the presence of lone pairs and nuclear shells in these areas.

Additionally, the oxygen atoms within the carbonyl groups exhibit a distinctive blue color, indicating the presence of more diffuse electron clouds surrounding them. The blue regions around the carbonyl oxygen atoms in the LOL maps point toward potential electron-deficient zones between the valence shell and inner core. Conversely, high LOL values, depicted in red, correspond to areas of stronger electron localization, particularly

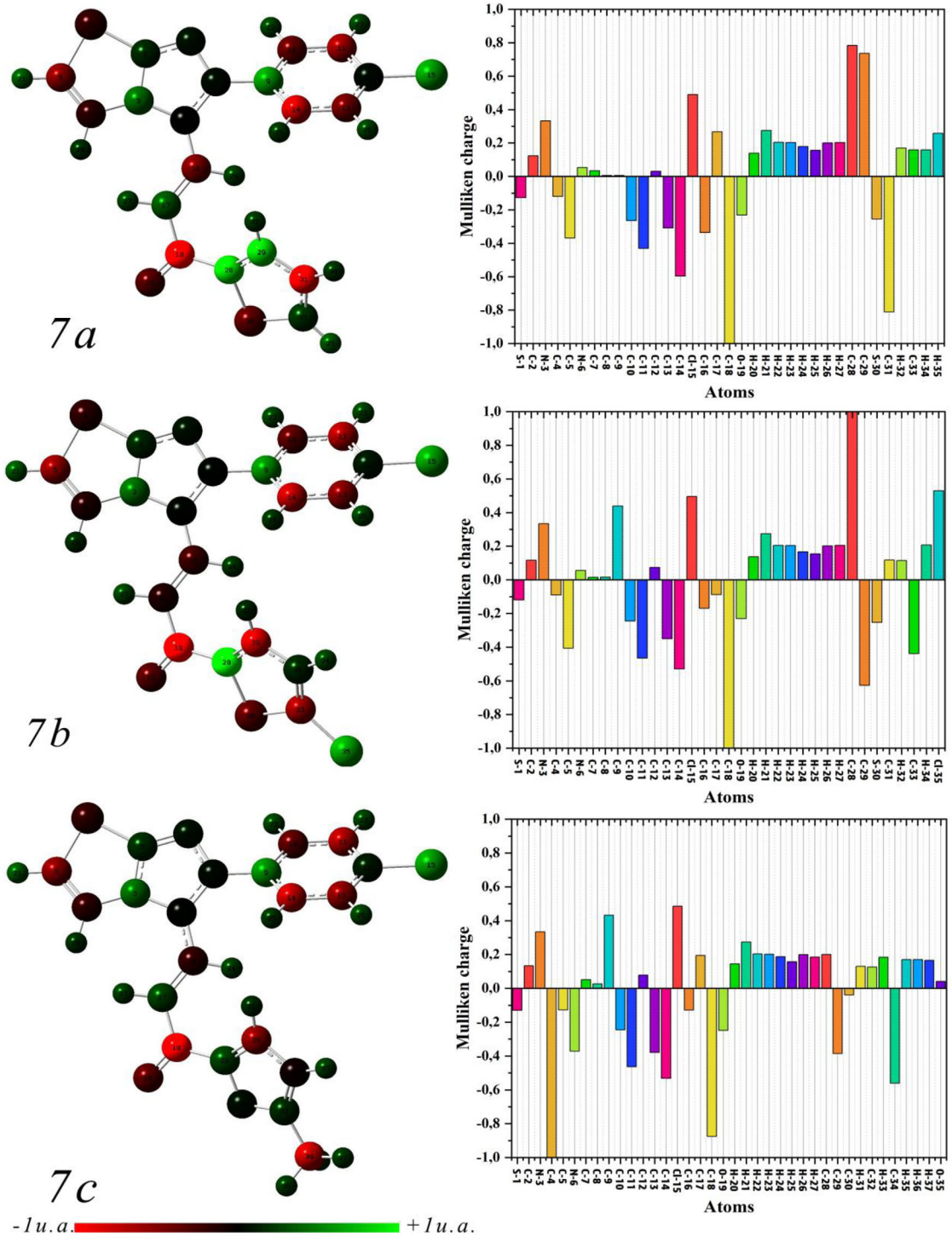

FIGURE 9 | Mulliken atomic charges designated by a color change on atoms of **7a–c**.

near the imidazothiazole nucleus, due to the covalent bonding within this part of the molecule [56].

The ELF and LOL maps suggest that the π-electrons in the conjugated chalcone system are relatively delocalized, further supporting the notion that these molecules can engage in π–π stacking interactions with biological macromolecules. This delocalization is important for stabilizing the molecules when interacting with biological targets, such as enzymes or cell membranes.

3.5.5 | QTAIM Analysis

QTAIM serves as a powerful and flexible tool within computational chemistry, especially designed to analyze non-covalent interactions (NCIs) in molecular systems. Utilizing principles of electron density and its derivatives, the reduced density gradient (RDG) method generates detailed 3D isosurfaces and scatter plots. These visual representations offer valuable insights into the spatial arrangement and strength of both attractive (such as van der Waals [VDW] forces and

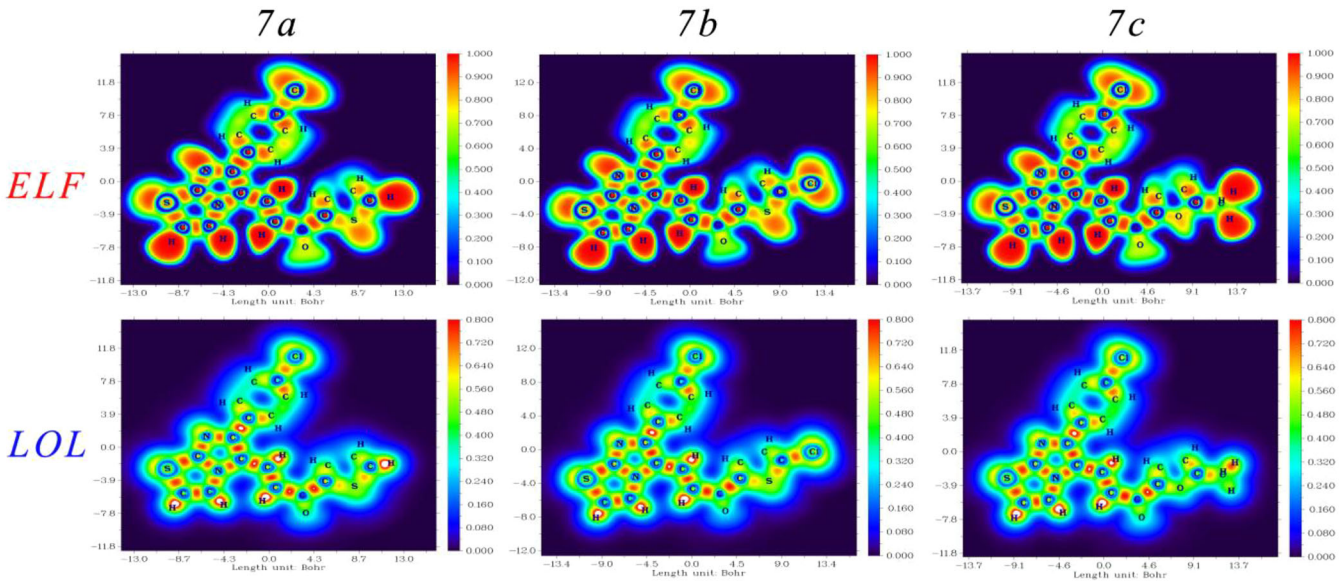

FIGURE 10 | ELF and LOL maps of **7a**–**c**. ELF, electron localization function; LOL, localized orbital locator.

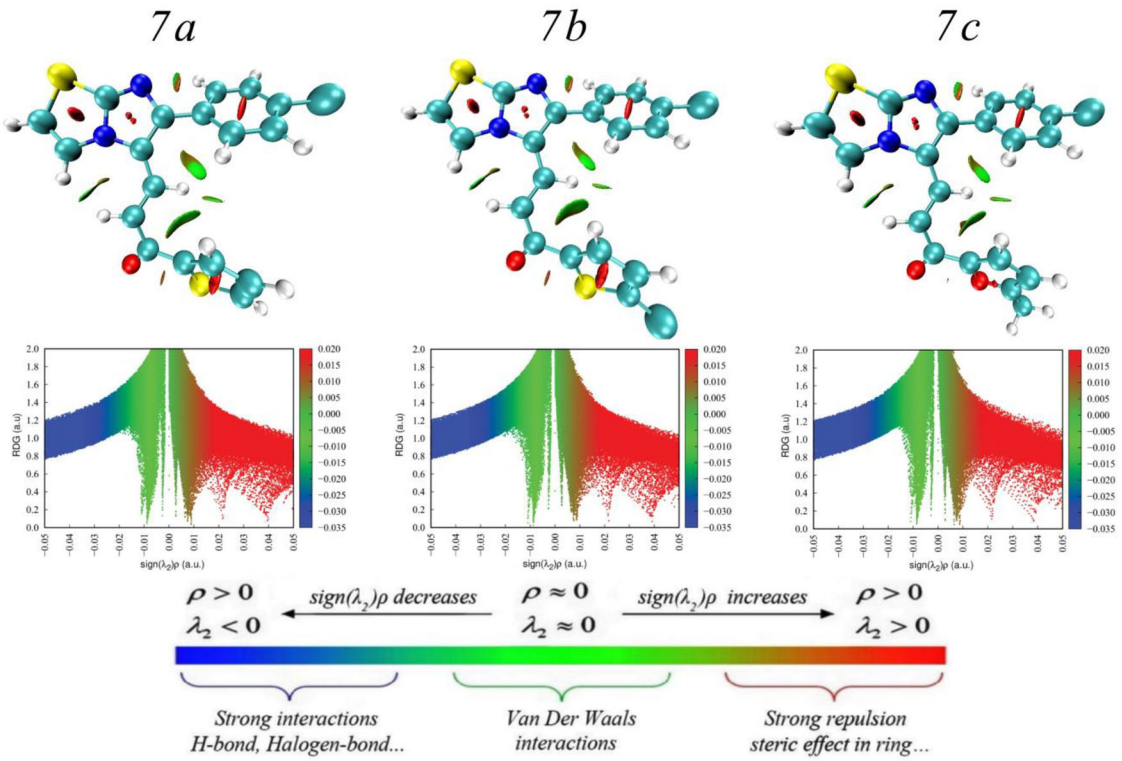

FIGURE 11 | NCI and RDG plot of **7a**–**c**. RDG, reduced density gradient.

hydrogen bonding) and repulsive interactions, like steric effects [57].

In this study, NCIs were examined and visualized through QTAIM molecular plots (Figure 11). The analyzed compounds displayed a variety of intra-molecular interactions, particularly VDW forces represented by (H…H) linkages with sign($\lambda 2$)ρ values (<−0.01 a.u.), along with (N…H) interactions. These interactions were marked by green spikes in the plots. Moreover, red regions observed within the cores of the imidazole, thiophene, and thiazole rings indicate substantial steric repulsion, characterized by peaks at positive sign($\lambda 2$)ρ values (>0.02 a.u) [58].

3.6 | Antibacterial Activity

The antibacterial activity of compounds **7a**–**c** was evaluated by determining their MIC and MBC against four bacterial strains: *P.*

TABLE 3 | The minimum inhibitory concentrations (MICs) and minimum bactericidal concentration (MBCs) in mg/mL of the studied compounds.

Bacterial strains	7a		7b		7c	
	MBC	MIC	MBC	MIC	MBC	MIC
P. aeruginosa	3.2	1.4	1.2	1	3.2	1.6
S. aureus	3.2	1.6	1.2	1	1.6	1.2
E. coli	1.4	1.2	1.2	1	1.4	1.2
K. pneumoniae	3.2	1.6	1.6	1.4	1.6	1.4

aeruginosa, S. aureus, *E. coli*, and *K. pneumoniae*. As reported in Table 3, the compounds exhibited varying degrees of antibacterial efficacy, with compound **7b** demonstrating the most notable activity, particularly against *E. coli* and *P. aeruginosa*, with MIC values around 1 mg/mL; these results indicate that the compounds possess a degree of inhibitory potential. Compound **7b**, in particular, showed measurable effects at relatively low concentrations, which may be attributed to the presence of a chlorine atom attached to the thiophene group. This structural feature may enhance the compound's interaction with bacterial membranes, contributing to its bactericidal effect. Compounds **7a** and **7c**, though showing activity, required higher concentrations to achieve inhibition, with less pronounced effects against *S. aureus* and *K. pneumoniae*. These observations suggest that structural variations, particularly in functional groups, may influence the efficacy of the compounds, and further structural optimization could potentially enhance their antibacterial properties.

In comparison with other studies, the MIC values for compound **7b** (1 mg/mL) align favorably with those reported for other synthetic antibacterial agents. For instance, Khatoon et al. [59] investigated 2,3-dichloroquinoxaline derivatives, and the most effective derivatives exhibited MIC values between 2.5 and 5 mg/mL against *Bacillus pumilus*, *E. coli*, *Salmonella Typhimurium*, and *Enterobacter aerogenes*. Similarly, Dadou et al. [60] evaluated chalcone-based imidazo[2,1-b]thiazole derivatives, where compound ITC-2 showed antibacterial activity with MICs of 500 μg/mL against *E. coli* and 200 μg/mL against *P. aeruginosa*. Moreover, Koudad et al. [61] reported that imidazopyridine Schiff base derivatives exhibited MIC values as low as 50 μg/mL against *P. aeruginosa* and *E. coli*. Comparatively, Erol et al. [62] demonstrated the antibacterial activity of benzoxazole derivatives with MICs ranging from 16 to 64 μg/mL against *S. aureus*. Çelik et al. [63] synthesized triazole-based compounds, where the most potent derivative showed MIC values between 312 and 5000 μg/mL against various bacterial strains.

The comparison highlights that although compound **7b** demonstrates notable antibacterial activity, its MIC values are higher than some more potent compounds in the literature, indicating room for further optimization. However, the observed activity of **7b** against multiple strains suggests its potential as a promising scaffold for the development of novel antibacterial agents.

3.7 | Antibiofilm Activity

The ability of compounds **7a**–**c** to inhibit biofilm formation was tested across various bacterial strains (Figure 12), and the findings are presented in Table 4. The results obtained reveal a generalized capacity of compounds **7a**–**c** to inhibit biofilm formation across multiple bacterial strains. In Well 3, which contained a concentration of 0.8 mg/mL, bacterial growth was observed, but no biofilm was detectable for any of the strains exposed to the three compounds. This antibiofilm effect was particularly noticeable with compound **7b**, which was able to inhibit biofilm formation at concentrations as low as 0.4 mg/mL for *P. aeruginosa*, *S. aureus*, and *E. coli* strains. The chlorine atom attached to the thiophene ring in compound **7b** may play a role in enhancing its ability to penetrate biofilm matrices and disrupt quorum sensing [64].

FIGURE 12 | Example of *Pseudomonas aeruginosa* biofilm in the presence of decreasing concentrations of **7a**.

Compound **7a** showed some efficacy in inhibiting biofilm formation, particularly against *S. aureus* and *E. coli*, though it was less effective than **7b**. In contrast, **7c** displayed antibiofilm activity only against *E. coli*, with no observable effects on *P. aeruginosa* or *S. aureus*.

These findings suggest a variation in the antibiofilm potential of the compounds depending on the bacterial strain and the concentration of the compound used. Although the antibiofilm activities are encouraging, further investigation would be needed to optimize the compounds for stronger biofilm disruption capabilities.

3.8 | Molecular Docking Analysis

Molecular docking simulations were performed to evaluate the binding affinity of the synthesized compounds against the DNA gyrase subunit B of *E. coli* (strain K12). DNA gyrase is a key enzyme involved in bacterial DNA replication, and inhibiting its function can lead to the suppression of bacterial growth, making it a significant target for antibiotic development. By assessing the interaction of these compounds with the enzyme, this research aims to identify potential inhibitors that could be developed as antibacterial agents [65].

TABLE 4 | Antibiofilm activity of **7a–c** against various bacterial strains.

Conc. (mg/mL)		3.2	1.6	0.8	0.4	0.2	0.1	0.05	0.025	0.0125	T+	T⁻
7a	*P. aeruginosa*	−	−	−	+	+	+	+	+	+	+	−
	S. aureus	−	−	−	−	+	+	+	+	+	+	−
	E. coli	−	−	−	−	+	+	+	+	+	+	−
	K. pneumoniae	−	−	−	+	+	+	+	+	+	+	−
7b	*P. aeruginosa*	−	−	−	−	+	+	+	+	+	+	−
	S. aureus	−	−	−	−	+	+	+	+	+	+	−
	E. coli	−	−	−	−	+	+	+	+	+	+	−
	K. pneumoniae	−	−	−	+	+	+	+	+	+	+	−
7c	*P. aeruginosa*	−	−	−	+	+	+	+	+	+	+	−
	S. aureus	−	−	−	+	+	+	+	+	+	+	−
	E. coli	−	−	−	−	+	+	+	+	+	+	−
	K. pneumoniae	−	−	−	+	+	+	+	+	+	+	−

Note: "−" means no biofilm; "+" means the presence of biofilm; "T^{+}" means MHB with inoculum as the positive control; "T^{-}" means MHB with DMSO as the negative control.

TABLE 5 | Docking scores of **7a–c** against DNA gyrase subunit B of *Escherichia coli* (strain K12).

Molecules	Docking score (Kcal/mol)
7a	−9.0
7b	−9.2
7c	−9.3

The docking scores, presented in Table 5, reveal the interaction dynamics between the synthesized compounds and DNA gyrase. Compounds **7a–c** exhibited promising binding affinities, ranging from −9.0 to −9.3 kcal/mol. These scores suggest robust interactions with amino acid residues within the enzyme's active site, potentially impeding its functional integrity [66].

The interaction analysis reveals crucial insights into how these molecules engage with the enzyme's active site. Each compound demonstrates a unique interaction profile, which is likely to influence its binding affinity and potential inhibitory activity. **7a** (Figure 13a, 13b) demonstrates a robust interaction profile, forming hydrogen bonds with VAL120 and ASN46. The interaction with ASN46 is particularly significant, as it is a key residue in the ATP-binding site of DNA gyrase. Mutations at ASN46 are known to reduce inhibitor affinity and catalytic activity, highlighting the importance of maintaining this interaction. Additionally, **7a** establishes pi–sigma interactions with ILE78, a residue critical for ATPase activity, and pi–alkyl interactions with PRO79, which contribute to the structural stabilization of the binding pocket. The pi–cation stacking with LYS103 and multiple VDW interactions further enhance the binding stability of **7a**, resulting in a strong docking score. Collectively, these interactions underscore the potential of **7a** as a DNA gyrase inhibitor. **7b** (Figure 13c, 13d) engages in a diverse array of interactions within the active site, including pi–pi T-shaped interactions with GLY77 and TYR109, amide–pi stacked interactions with ASN46, and pi–cation interactions with LYS103. The involvement of GLY77 and ILE78 is particularly noteworthy, as mutations at these residues can significantly reduce ATPase activity, a critical function of GyrB. The pi–alkyl interactions with PRO79 and ILE78, coupled with VDW interactions, anchor 7b effectively within the binding pocket. Its docking score of −9.2 kcal/mol reflects the stability and strength of these interactions, making **7b** a promising candidate for further development. **7c** (Figure 13e, 13f), exhibits the most comprehensive interaction profile, forming pi–cation interactions with ARG76 and ARG136. These residues are critical to the active site's negatively charged environment, and ARG136, in particular, is a frequently mutated residue in novobiocin-resistant strains. By interacting with ARG136, **7c** may retain efficacy even in the presence of certain resistance mechanisms. Additional interactions include pi–alkyl bonds with PRO79, pi–sigma interactions with ILE78, and VDW interactions with GLY77. These interactions contribute to the compound's docking score of −9.3 kcal/mol, emphasizing its potential as a potent inhibitor of DNA gyrase [67a, 67b, 67c].

The molecular docking results align well with experimental data, demonstrating the compounds biological potentials. However, further structural optimization may enhance their antibacterial efficacy. These preliminary findings are encouraging; they highlight the potential of these imidazo[2, 1-b]thiazole-based chalcone derivatives as DNA gyrase inhibitors and lay a groundwork for subsequent research into their mechanism of action against bacterial infections [26].

4 | Conclusion

This study presents a simple and efficient method for synthesizing novel imidazo[2, 1-b] thiazole-based chalcones from readily available reactants. The green chemistry metrics demonstrated that the synthesis process is environmentally friendly, with high

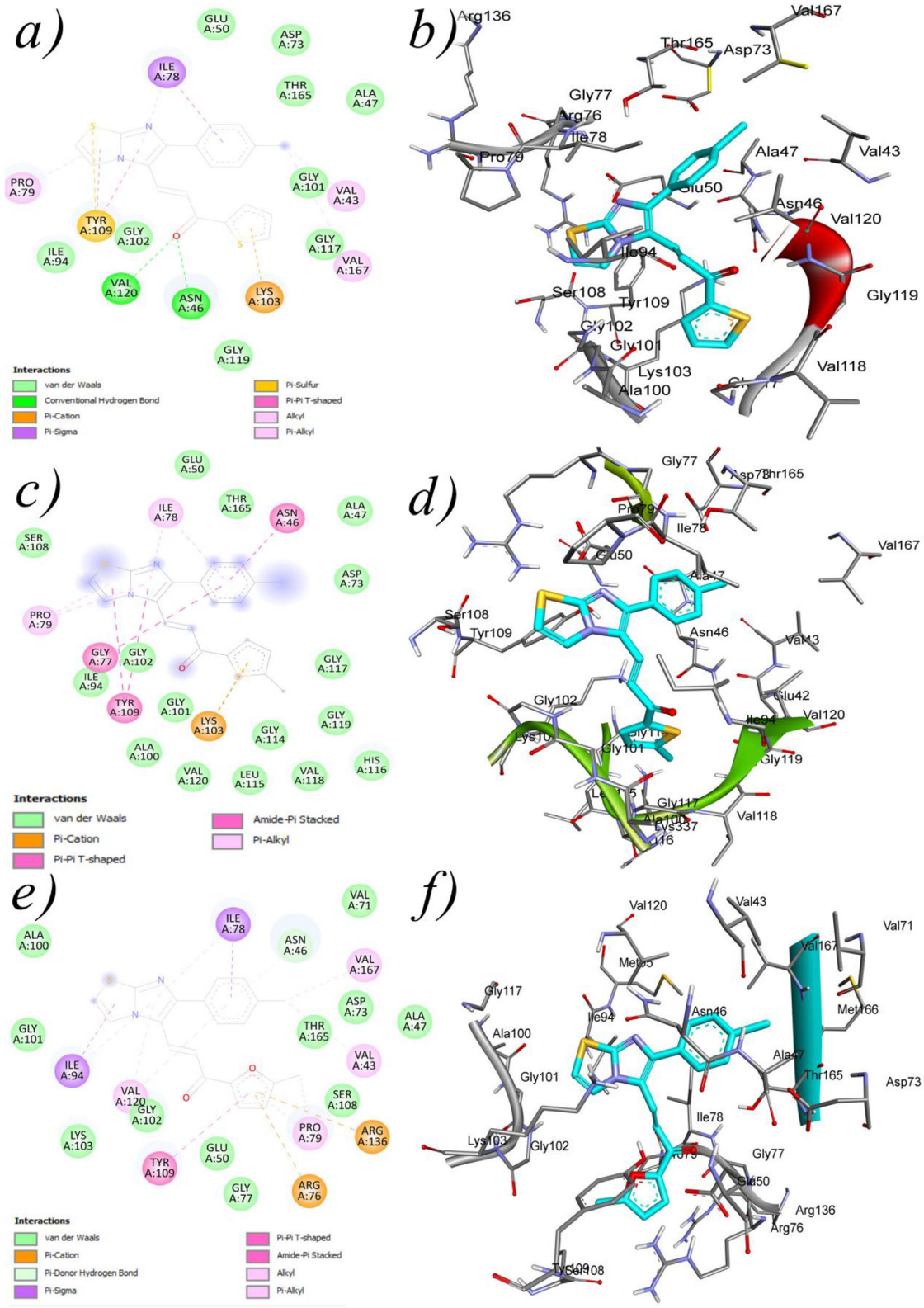

FIGURE 13 | FIGURE 13 2D and 3D views of interaction between 7a–c and protein (PDB ID: 4PRX).

AE and low waste generation. The synthesized compounds were characterized using various techniques, including ^{1}H and ^{13}C NMR, LC–MS, and FT-IR. The theoretical FT-IR and NMR analyses correlated well with the experimental findings. Computational studies using DFT/B3LYP/6-311++G(d,p) basis set provided insight into the compounds' reactivity and behavior. Furthermore, these compounds were evaluated for their antibacterial and antibiofilm activities, with promising results; particularly, **7b** demonstrated superior activity with an MIC of 1 mg/mL against *E. coli* and *P. aeruginosa*, outperforming

other compounds. Compound **7b** also showed strong antibiofilm activity, with complete inhibition of biofilm formation at a concentration of 0.4 mg/mL, highlighting its potential as a potent antibiofilm agent. Molecular docking studies supported these findings, with **7b** exhibiting a binding affinity score of −9.2 kcal/mol with DNA gyrase subunit B, indicating robust interactions with bacterial targets.

However, further structural optimization and investigations are still required to enhance the compounds' therapeutic potential and fully explore their spectrum of biological activities. Future studies should focus on improving their efficacy, optimizing pharmacokinetic properties, and expanding investigations to other pathogenic strains.

Author Contributions

Mohamed Azzouzi: validation, writing–original draft. **Mohamed El Boutaybi**: investigation, methodology. **El Hassan El Majidi**: resources, formal analysis. **Mohammed Timinouni**: resources, methodology. **Lamiae El Khattabi**: software, visualization. **Khadim Dioukhane**: software, methodology. **Sofia Fait**: software, formal analysis. **Adyl Oussaid**: validation, supervision, writing.

Acknowledgments

The authors thank their respective institutions for providing the necessary facility to complete this work.

Conflicts of Interest

The authors declare no conflicts of interest.

Data Availability Statement

The data that support the findings of this study are available from the corresponding author upon reasonable request.

References

1. A. E. Rashad, A. E. Mahmoud, and M. M. Ali, "Synthesis and Anticancer Effects of Some Novel Pyrazolo[3,4-d]Pyrimidine Derivatives by Generating Reactive Oxygen Species in Human Breast Adenocarcinoma Cells," *European Journal of Medicinal Chemistry* 46 (2011): 1019–1026.

2. M. L. Fascio, M. I. Errea, and N. B. D'Accorso, "Imidazothiazole and Related Heterocyclic Systems. Synthesis, Chemical and Biological Properties," *European Journal of Medicinal Chemistry* 90 (2015): 666–683.

3. S. P. Shaik, M. V. P. S. Vishnuvardhan, F. Sultana, et al., "Design and Synthesis of 1,2,3-Triazolo Linked Benzo[d]imidazo[2,1-b]thiazole Conjugates as Tubulin Polymerization Inhibitors," *Bioorganic & Medicinal Chemistry* 25 (2017): 3285–3297.

4. [4a] C. M. A. Abdulla, M. Neetha, T. Aneeja, and G. Anilkumar, "Synthesis and Applications of Imidazothiazoles: An Overview," *ChemistrySelect* 5 (2020): 10374–10386. [4b] R. S. Kumar, S. Praveen, K. Shridharshini, M. Maruthamuthu, K. Mohanapriya, and A. Mythili, "Biological Applications of Imidazothiazole Scaffolds: A Current Review," *Journal of Advanced Chemical Sciences* 8 (2022): 756–769. [4c] I. Mishra, R. Mishra, S. Mujwar, P. Chandra, and N. Sachan, "A Retrospect on Antimicrobial Potential of Thiazole Scaffold," *Journal of Heterocyclic Chemistry* 57 (2020): 2304–2329. [4d] R. Gali, J. Banothu, M. Porika, R. Velpula, R. Bavantula, and S. Abbagani, "Synthesis and In Vitro Cytotoxic Activity of Novel Coumarinylimidazo[2,1-b]thiazole Derivatives," *RSC Advances* (2014): 53812–53819.

5. A. Andreani, A. Leoni, A. Locatelli, et al., "Potential Antitumor Agents. Part 291: Synthesis and Potential Coanthracyclinic Activity of Imidazo[2,1-b]thiazole Guanylhydrazones," *Bioorganic & Medicinal Chemistry* 8 (2000): 2359–2366.

6. [6a] A. Kamal, D. Dastagiri, M. J. Ramaiah, et al., "Design and Synthesis of Imidazo[2,1-b]thiazole Linked Triazole Conjugates: Microtubule-Destabilizing Agents," *European Journal of Medicinal Chemistry* 5 (2010): 1937–1947. [6b] J.-H. Park, M. I. El-Gamal, Y. S. Lee, and C.-H. Oh, "New Imidazo[2,1-b]thiazole Derivatives: Synthesis, In Vitro Anticancer Evaluation, and In Silico Studies," *European Journal of Medicinal Chemistry* 46 (2011): 5769–5777. [6c] W.-T. Li, D.-R. Hwang, J.-S. Song, et al., "Synthesis and Biological Evaluation of 2-Amino-1-Thiazolyl Imidazoles as Orally Active Anticancer Agents," *Investigational New Drugs* 30 (2012): 164–175.

7. N. U. Güzeldemirci and Ö. Küçükbasmacı, "Synthesis and Antimicrobial Activity Evaluation of New 1,2,4-Triazoles and 1,3,4-Thiadiazoles Bearing Imidazo[2,1-b]thiazole Moiety," *European Journal of Medicinal Chemistry* 45 (2010): 63–68.

8. J. S. Barradas, M. I. Errea, N. B. D'Accorso, C. S. Sepúlveda, and E. B. Damonte, "Imidazo[2,1-b]thiazole Carbohydrate Derivatives: Synthesis and Antiviral Activity Against Junin Virus, Agent of Argentine Hemorrhagic Fever," *European Journal of Medicinal Chemistry* 46 (2011): 259–264.

9. [9a] T. Juspin, M. Laget, T. Terme, N. Azas, and P. Vanelle, "TDAE-Assisted Synthesis of New Imidazo[2,1-b]thiazole Derivatives as Anti-Infectious Agents," *European Journal of Medicinal Chemistry* 45 (2010): 840–845. [9b] J. K. Malik, H. Soni, and A. K. Singhai, "Synthesis, Characterization and Evaluation for Antifungal Activity of Substituted Diaryl Imidazo [2, 1, b]-benzothiazole," *Journal of Pharmacy Research* 7 (2013): 39–46.

10. R. Budriesi, P. Ioan, A. Locatelli, et al., "Imidazo[2,1-b]thiazole System: A Scaffold Endowing Dihydropyridines With Selective Cardiodepressant Activity," *Journal of Medicinal Chemistry* 51 (2008): 1592–1600.

11. V. B. Jadhav, M. V. Kulkarni, V. P. Rasal, S. S. Biradar, and M. D. Vinay, "Synthesis and Anti-Inflammatory Evaluation of Methylene Bridged Benzofuranyl Imidazo[2,1-b][1,3,4]thiadiazoles," *European Journal of Medicinal Chemistry* 43 (2008): 1721–1729.

12. D. C. Cole, J. R. Stock, W. J. Lennox, et al., "Discovery of N1-(6-Chloroimidazo[2,1-b][1,3]thiazole-5-Sulfonyl)tryptamine as a Potent, Selective, and Orally Active 5-HT(6) Receptor Agonist," *Journal of Medicinal Chemistry* 50 (2007): 5535–5538.

13. [13a] J. A. Laurie, C. G. Moertel, T. R. Fleming, et al., "Surgical Adjuvant Therapy of Large-Bowel Carcinoma: An Evaluation of Levamisole and the Combination of Levamisole and Fluorouracil. The North Central Cancer Treatment Group and the Mayo Clinic," *Journal of Clinical Oncology* 7 (1989): 1447–1456. [13b] A. H. M. Raeymaekers, F. T. N. Allewijn, J. Vandenberk, P. J. A. Demoen, T. T. T. Van Offenwert, and P. A. J. Janssen, "Novel Broad-Spectrum Anthelmintics. Tetramisole1 and Related Derivatives of 6-Arylimidazo[2,1-b]thiazole," *Journal of Medicinal Chemistry* 9 (1966): 545–551.

14. [14a] A. Kamal, M. K. Reddy, and A. Viswanath, "The Design and Development of Imidazothiazole–Chalcone Derivatives as Potential Anticancer Drugs," *Expert Opinion on Drug Discovery* 8 (2013): 289–304. [14b] A. Kamal, M. Balakrishna, V. L. Nayak, T. B. Shaik, S. Faazil, and V. D. Nimbarte, "Design and Synthesis of Imidazo[2,1-b]thiazole–Chalcone Conjugates: Microtubule-Destabilizing Agents," *Chemmedchem* 9 (2014): 2766–2780.

15. [15a] C. Zhuang, W. Zhang, C. Sheng, W. Zhang, C. Xing, and Z. Miao, "Chalcone: A Privileged Structure in Medicinal Chemistry," *Journal of Medicinal Chemistry* 117 (2017): 7762–7810. [15b] C. B. Vu, J. E. Bemis, J. S. Disch, et al., "Discovery of Imidazo[1,2-b]thiazole Derivatives as Novel SIRT1 Activators," *Journal of Medicinal Chemistry* 52 (2009): 1275–1283.

16. [16a] R. M. Sbenati, M. H. Semreen, A. M. Semreen, M. K. Shehata, F. M. Alsaghir, and M. I. El-Gamal, "Evaluation of Imidazo[2,1–b]thiazole-Based Anticancer Agents in One Decade (2011–2020): Current Status and Future Prospects," *Bioorganic & Medicinal Chemistry* 29 (2021): 115897.

[16b] M. A. Shareef, I. Khan, B. N. Babu, and A. Kamal, "A Comprehensive Review on the Therapeutic Versatility of Imidazo [2,1-b]thiazoles," *Current Medicinal Chemistry* 27 (2020): 6864–6887.

17. M. Hagar, H. A. Ahmed, G. Aljohani, and O. A. Alhaddad, "Investigation of Some Antiviral N-Heterocycles as COVID 19 Drug: Molecular Docking and DFT Calculations," *International Journal of Molecular Sciences* 21 (2020): 3922.

18. N. Mardirossian and M. Head-Gordon, "Thirty Years of Density Functional Theory in Computational Chemistry: An Overview and Extensive Assessment of 200 Density Functionals", *Molecular Physics* 115 (2017): 2315–2372.

19. O. Azougagh, S. Essayeh, N. Achalhi, et al., "New Benzyltriethylammonium/Urea Deep Eutectic Solvent: Quantum Calculation and Application to Hyrdoxylethylcellulose Modification," *Carbohydrate Polymers* 276 (2022): 118737.

20. M. Azzouzi, Z. E. Ouafi, O. Azougagh, et al., "Design, Synthesis, and Computational Studies of Novel Imidazo[1,2-a]pyrimidine Derivatives as Potential Dual Inhibitors of hACE2 and Spike Protein for Blocking SARS-CoV-2 Cell Entry," *Journal of Molecular Structure 1285* (2023): 135525.

21. P. C. Agu, C. A. Afiukwa, O. U. Orji, et al., "Molecular Docking as a Tool for the Discovery of Molecular Targets of Nutraceuticals in Diseases Management," *Scientific Reports* 13 (2023): 13398.

22. T. Lu and F. Chen, "Multiwfn: A Multifunctional Wavefunction Analyzer," *Journal of Computational Chemistry* 33 (2012): 580–592.

23. M. M. Bazargani and J. Rohloff, "Antibiofilm Activity of Essential Oils and Plant Extracts against Staphylococcus aureus and Escherichia coli biofilms," *Food Control* 61 (2016): 156–164.

24. M. R. Moreira, A. G. Ponce, C. E. del Valle, and S. I. Roura, "Inhibitory Parameters of Essential Oils to Reduce a Foodborne Pathogen," *LWT—Food Science and Technology* 38 (2005): 565–570.

25. apos, G. Toole, H. B. Kaplan, and R. Kolter, "Biofilm Formation as Microbial Development," *Annual Review of Microbiology* 54 (2000): 49–79.

26. J. M. Carpio Arévalo and J. C. Amorim, "An In-Silico Analysis Reveals 7,7′-Bializarin as a Promising DNA Gyrase B Inhibitor on Gram-Positive and Gram-Negative Bacteria," *Computers in Biology and Medicine* 135 (2021): 104626.

27. O. Trott and A. J. Olson, "AutoDock Vina: Improving the Speed and Accuracy of Docking With a New Scoring Function, Efficient Optimization, and Multithreading," *Journal of Computational Chemistry* 31 (2010): 455–461.

28. M. Azzouzi, O. Azougagh, A. A. Ouchaoui, et al., "Synthesis, Characterizations, and Quantum Chemical Investigations on Imidazo[1,2-a]pyrimidine-Schiff Base Derivative: (E)-2-Phenyl-N-(thiophen-2-ylmethylene)imidazo[1,2-a]pyrimidin-3-Amine," *ACS Omega* 9 (2024): 837–857.

29. M. A. Shareef, G. P. Devi, S. Rani Routhu, C. G. Kumar, A. Kamal, and B. N. Babu, "New Imidazo[2,1-b]thiazole-Based Aryl Hydrazones: Unravelling Their Synthesis and Antiproliferative and Apoptosis-Inducing Potential," *RSC Medicinal Chemistry* 11 (2020): 1178–1184.

30. [30a] T. V. T. Phan, C. Gallardo, and J. Mane, "Green Motion: A New and Easy to Use Green Chemistry Metric From Laboratories to Industry," *Green Chemistry* 17 (2015): 2846–2852. [30b] R. A. Sheldon, "The E Factor at 30: A Passion for Pollution Prevention," *Green Chemistry* 25 (2023): 1704–1728.

31. [31a] D. J. C. Constable, A. D. Curzons, and V. L. Cunningham, "Metrics to 'Green' Chemistry—Which are the Best?," *Green Chemistry* 4 (2002): 521–527. [31b] J. Andraos, "Unification of Reaction Metrics for Green Chemistry: Applications to Reaction Analysis," *Organic Process Research & Development* 9 (2005): 519–519. [31c] R. A. Sheldon, "Metrics of Green Chemistry and Sustainability: Past, Present, and Future," *ACS Sustainable Chemistry & Engineering* 6 (2018): 32–48.

32. M. Raja, R. R. Muhamed, S. Muthu, and M. Suresh, "Synthesis, Spectroscopic (FT-IR, FT-Raman, NMR, UV–Visible), First Order Hyperpolarizability, NBO and Molecular Docking Study of (E)-1-(4-Bromobenzylidene)semicarbazide," *Journal of Molecular Structure* 1128 (2017): 481–492.

33. S. Srinivasan, T. A. Hajam, S. Sathish, and R. K. Grewal, "Synthesis, Quantum Mechanical Calculations, Molecular Docking, Hirshfeld Surface analysis and ADMET Estimation Studies of (E)-3-(Anthracene-10-yl)-1-(Napthalen-1-yl)prop-2-En-1-One," *Journal of Molecular Structure* 1269 (2022): 133748.

34. L. V. de Freitas, C. C. P. da Silva, J. Ellena, L. A. S. Costa, and N. A. Rey, "Structural and Vibrational Study of 8-Hydroxyquinoline-2-Carboxaldehyde Isonicotinoyl Hydrazone – A Potential Metal–Protein Attenuating Compound (MPAC) for the Treatment of Alzheimer's Disease," *Spectrochimica Acta Part A: Molecular and Biomolecular Spectroscopy* 116 (2013): 41–48.

35. D. Rajaraman, G. Sundararajan, N. K. Loganath, and K. Krishnasamy, "Synthesis, Molecular Structure, DFT Studies and Antimicrobial Activities of Some Novel 3-(1-(3,4-Dimethoxyphenethyl)-4,5-Diphenyl-1H-Imidazol-2-yl)-1H-Indole Derivatives and Its molecular Docking Studies," *Journal of Molecular Structure* 1127 (2017): 597–610.

36. Z. Asadi, M. D. Esrafili, E. Vessally, M. Asnaashariisfahani, S. Yahyaei, and A. Khani, "A Structural Study of Fentanyl by DFT Calculations, NMR and IR Spectroscopy," *Journal of Molecular Structure* 1128 (2017): 552–562.

37. P. G. Patil, R. Melavanki, S. B. Radder, et al., "Synthesis, Structural Characterizations, and Quantum Chemical Investigations on 1-(3-Methoxy-Phenyl)-3-Naphthalen-1-Yl-Propenone," *ACS Omega* 6 (2021): 25982–25995.

38. M. Raja, R. Raj Muhamed, S. Muthu, and M. Suresh, "Synthesis, Spectroscopic (FT-IR, FT-Raman, NMR, UV–Visible), NLO, NBO, HOMO-LUMO, Fukui Function and Molecular Docking Study of (E)-1-(5-Bromo-2-Hydroxybenzylidene)semicarbazide," *Journal of Molecular Structure* 1141 (2017): 284–298.

39. S. P. Biswal, P. Hota, M. R. Dash, and P. K. Misra, "Theoretical Interpretation of Electron Delocalization Potential of the Substituent in O-Hydroxynaphthalidene-P-Substituted Anilines for Prospective Molecular Electronics Applications," *Discover Molecules* 1 (2024): 2.

40. V. Vijayakumar, A. Prabakaran, N. Radhakrishnan, S. Muthu, C. Rameshkumar, and E. I. Paulraj, "Synthesis, Characterization, Spectroscopic Studies, DFT and Molecular Docking Analysis of N4, N4′-Dibutyl-3, 3′-Diaminobenzidine," *Journal of Molecular Structure* 1179 (2019): 325–335.

41. I. Azad, T. Khan, R. Ahmad, A. Kamal, A. R. Khan, and M. Nasibullah, "A Simplistic Approach for Preparation of Alkylidenemalononitrile Derivatives: Characterization, In silico Studies, Quantum Chemical Evaluation, Molecular Docking, and In Vitro Biological Activity Evaluation," *Journal of Molecular Structure* 1228 (2021): 129451.

42. P. Vennila, G. Venkatesh, Y. Sixto-López, et al., "Synthesis, Spectroscopic Characterization, Molecular Docking Studies and DFT Calculation of Novel Mannich Base 1-((4-Ethylpiperazin-1-yl)(2-Hydroxyphenyl)methyl)naphthalen-2-ol," *Journal of Molecular Structure 1246* (2021): 131164.

43. W. Daoudi, M. Azzouzi, M. Aaddouz, et al., "Synthesis, Characterization, DFT, ADMET, MD Analysis and Molecular Docking of C-3 Functionalized Imidazo[1,2-a]pyridine Motifs," *Journal of Molecular Structure* 1312 (2024): 138658.

44. Y. Kubota, S. Tanaka, K. Funabiki, and M. Matsui, "Synthesis and Fluorescence Properties of Thiazole–Boron Complexes Bearing a *β*-Ketoiminate Ligand," *Organic Letters* 14 (2012): 4682–4685.

45. Ž. B. Milanović, D. S. Dimić, E. H. Avdović, et al., "Synthesis and Comprehensive Spectroscopic (X-Ray, NMR, FTIR, UV–Vis), Quantum Chemical and Molecular Docking Investigation of 3-Acetyl-4-Hydroxy-2-Oxo-2H-Chromen-7-yl Acetate," *Journal of Molecular Structure* 1225 (2021): 129256.

46. I. Azad, Y. Akhter, T. Khan, et al., "Synthesis, Quantum Chemical Study, AIM Simulation, In Silico ADMET Profile Analysis, Molecular

Docking and Antioxidant Activity Assessment of Aminofuran Derivatives," *Journal of Molecular Structure* 1203 (2020): 127285.

47. R. A. Costa, E. S. A. Junior, G. B. P. Lopes, et al., "Structural, Vibrational, UV–Vis, Quantum-Chemical Properties, Molecular Docking and Anti-Cancer Activity Study of Annomontine and N-Hydroxyannomontine β-Carboline Alkaloids: A Combined Experimental and DFT Approach," *Journal of Molecular Structure* 1171 (2018): 682–695.

48. M. A. Mumit, T. K. Pal, M. A. Alam, M. A.-A.-A.-A. Islam, S. Paul, and M. C. Sheikh, "DFT Studies on Vibrational and Electronic Spectra, HOMO–LUMO, MEP, HOMA, NBO and Molecular Docking Analysis of Benzyl-3-N-(2,4,5-Trimethoxyphenylmethylene) hydrazinecarbodithioate," *Journal of Molecular Structure* 1220 (2020): 128715.

49. A. Jeelani, S. Muthu, B. R. Raajaraman, and S. Sevvanthi, "Spectroscopic, Quantum Chemical Calculations, and Molecular Docking Analysis of 3-Chlorophenyl Boronic Acid," *Spectroscopy Letters* 53 (2020): 778–792.

50. D. Rajaraman, L. A. Anthony, P. Nethaji, and R. Vallangi, "One-Pot Synthesis, NMR, Quantum Chemical Approach, Molecular Docking Studies, Drug-Likeness and In-Silico ADMET Prediction of Novel 1-(2,3-Dihydrobenzo[b][1,4]dioxin-6-yl)-2-(Furan-2-yl)-4,5-Diphenyl-1H-Imidazole Derivatives," *Journal of Molecular Structure* 1273 (2023): 134314.

51. A. G. Al-Sehemi, A. Irfan, A. M. Asiri, and Y. A. Ammar, "Molecular Design of New Hydrazone Dyes for Dye-Sensitized Solar Cells: Synthesis, Characterization and DFT Study," *Journal of Molecular Structure* 1019 (2012): 130–134.

52. J. Geethapriya, A. Shanthidevi, M. Arivazhagan, N. Elangovan, and R. Thomas, "Synthesis, Structural, DFT, Quantum Chemical Modeling and Molecular Docking Studies of (E)-4-(((5-Methylfuran-2-yl) methylene)amino) Benzenesulfonamide From 5-Methyl-2-Furaldehyde and Sulfanilamide," *Journal of the Indian Chemical Society* 99 (2022): 100418.

53. H. M. Abd El-Lateef, M. M. Khalaf, A. A. Amer, M. Kandeel, A. A. Abdelhamid, and A. Abdou, "Synthesis, Characterization, Antimicrobial, Density Functional Theory, and Molecular Docking Studies of Novel Mn(II), Fe(III), and Cr(III) Complexes Incorporating 4-(2-Hydroxyphenyl Azo)-1-Naphthol (Az)," *ACS Omega* 8 (2023): 25877–25891.

54. A. S. M. Al-Janabi, A. O. Elzupir, and T. A. Yousef, "Synthesis, Anti-Bacterial Evaluation, DFT Study and Molecular Docking as a Potential 3-Chymotrypsin-Like Protease (3CLpro) of SARS-CoV-2 Inhibitors of a Novel Schiff Bases," *Journal of Molecular Structure* 1228 (2021): 129454.

55. S. Janani, H. Rajagopal, S. Muthu, S. Aayisha, and M. Raja, "Molecular Structure, Spectroscopic (FT-IR, FT-Raman, NMR), HOMO-LUMO, Chemical Reactivity, AIM, ELF, LOL and Molecular Docking Studies on 1-Benzyl-4-(N-Boc-Amino)piperidine," *Journal of Molecular Structure* 1230 (2021): 129657.

56. S. SangeethaMargreat, S. Ramalingam, H. M. Al-Maqtari, et al., "Synthesis, Spectroscopic, Quantum Computation, Electronic, AIM, Wavefunction (ELF, LOL) and Molecular Docking Investigation on (E)-1-(2,5-Dichlorothiophen-3-yl)-3-(Thiophen-2-yl)-2-Propen-1-One," *Chemical Data Collections* 33 (2021): 100701.

57. K. S. Devi, P. Subramani, S. Parthiban, and N. Sundaraganesan, "One-Pot Synthesis, Spectroscopic Characterizations, Quantum Chemical Calculations, Docking and Cytotoxicity of 1-((Dibenzylamino)methyl) pyrrolidine-2,5-Dione," *Journal of Molecular Structure* 1203(2020): 127403.

58. P. Jeeva, S. Sudha, A. Rakić, D. Dimić, D. Ramarajan, and D. Barathi, "Structural, Spectroscopic, Quantum Chemical, and Molecular Docking Study Towards Cartilage Protein of (3E,3′E)-3,3′-(1,4-Phenylenebis(azanediyl))bis(cyclohex-2-En-1-One)," *Journal of Molecular Structure* 1274 (2023): 134429.

59. H. Khatoon, E. A. Malek, S. M. Mohd Faudzi, T. Khan, and O. S. Ahmed, "Synthesis of Quinoxaline Derivatives Using Different Solvent Systems, Their Potent Antibacterial Activities and Molecular Docking," *Results in Chemistry* 7 (2024): 101389.

60. S. Dadou, M. El Farkhani, C. Hamouti, et al., "Antimicrobial Activity and Molecular Docking Studies of Some Imidazo[2,1-b]thiazole Derivatives," *BIO Web of Conferences* 109 (2024): 01019.

61. M. Koudad, S. Dadou, F. Abrigach, et al., "Synthesis and Antimicrobial, Antioxidant, ADME-T, and Molecular Docking Studies of Imidazo[1,2-a]pyridine Derivatives," *Russian Journal of Organic Chemistry* 59 (2023): 1237–1247.

62. M. Erol, I. Celik, and G. Kuyucuklu, "Synthesis, Molecular Docking, Molecular Dynamics, DFT and Antimicrobial Activity Studies of 5-Substituted-2-(p-Methylphenyl)benzoxazole Derivatives," *Journal of Molecular Structure* 1234 (2021): 130151.

63. F. Çelik, R. Ustabaş, N. Süleymanoğlu, Ş. Direkel, H. İ. Güler, and Y. Ünver, "1,2,3-Triazole Derivative: Synthesis, Characterization, DFT, Molecular Docking Study and Antibacterial-Antileishmanial Activities," *Journal of the Indian Chemical Society* 98 (2021): 100105.

64. M. Gonzales, B. Kergaravat, P. Jacquet, et al., "Disrupting Quorum Sensing as a Strategy to Inhibit Bacterial Virulence in Human, Animal, and Plant Pathogens," *Pathogens and Disease* 82 (2024): ftae009.

65. O. Moussaoui, R. Bhadane, R. Sghyar, et al., "Novel Amino Acid Derivatives of Quinolines as Potential Antibacterial and Fluorophore Agents," *Scientia Pharmaceutica* 88 (2020): 57.

66. A. Zarkan, M. Matuszewska, S. B. Trigg, et al., "Inhibition of Indole Production Increases the Activity of Quinolone Antibiotics Against *E. coli* Persisters," *Scientific Reports* 10 (2020): 11742.

67. [67a] M. Durcik, D. Lovison, Ž. Skok, et al., "New N-Phenylpyrrolamide DNA Gyrase B Inhibitors: Optimization of Efficacy and Antibacterial Activity," *European Journal of Medicinal Chemistry* 154 (2018): 117–132. [67b] I. Shiriaev Dmitrii, A. Sofronova Alina, A. Berdnikovich Ekaterina, et al., "Nybomycin Inhibits Both Fluoroquinolone-Sensitive and Fluoroquinolone-Resistant *Escherichia coli* DNA Gyrase," *Antimicrobial Agents and Chemotherapy* 65 (2021): AAC.00777-20. [67c] F. Collin, S. Karkare, and A. Maxwell, "Exploiting Bacterial DNA Gyrase as a Drug Target: Current State and Perspectives," *Applied Microbiology and Biotechnology* 92 (2011): 479–497.

Supporting Information

Additional supporting information can be found online in the Supporting Information section.